

On the role of water activity on the formation of a protein-rich coffee ring in an evaporating multicomponent drop

Javier Martínez-Puig^{*1}, Gianluca D’Agostino², Ana Oña², and Javier Rodríguez-Rodríguez¹

¹Carlos III University of Madrid, Department of Thermal and Fluids Engineering, Leganés, 28911, Spain

²Centro Nacional de Biotecnología, Consejo Superior de Investigaciones Científicas CSIC, Madrid, Spain

Abstract

The coffee-ring effect is a universal feature of evaporating sessile droplets with pinned contact line, wherein solutes or particles are advected to the droplet’s edge due to evaporation-driven flows. While existing models have successfully described this phenomenon in particle-laden droplets, they often assume that hydrodynamics are decoupled from solute transport. This assumption breaks down in complex fluids, such as protein or polymeric solutions, where the solute can influence evaporation through changes in water activity. Here, we investigate model respiratory droplets primarily composed of water, salt, and a type of the glycoprotein mucin. Using fluorescence microscopy, we observe the formation of a well-defined protein ring at the droplet edge as water evaporates. The growth and morphology of this ring exhibit a strong dependence on ambient relative humidity (H_r), revealing dynamics that existing models cannot capture. Specifically, we find that protein accumulation at the edge is governed by the feedback between local solute concentration and evaporation rate. To account for this, we develop a minimal theoretical model based on the lubrication approximation, incorporating the coupling between hydrodynamics and solute transport through the evaporation rate. Our framework reproduces key features of the experimental observations and suggests a physical basis for the H_r -dependent stability and infectivity of respiratory droplets containing viruses.

1 Introduction

Since the seminal works by the Chicago group [7, 8], the coffee-ring effect (CRE) has garnered significant attention. In an evaporating sessile droplet, the pinning of the contact line imposes a radial outward flow to enforce mass conservation, transporting material from the center toward the edge. In particle-laden droplets, this advective flow carries particles to the contact line, resulting

^{*}Corresponding author: jmpuig@pa.uc3m.es

in the characteristic ring-shaped deposit that has been extensively studied through simplified models of the CRE. However, in more complex fluids, this transport involves not particles but solutes such as polymers, proteins, or salts. The evaporation of such complex fluids is relevant in many situations of practical interest (see for example, Kajiya *et al.* [21], Guo *et al.* [18], Mailleur *et al.* [26], Basu & Mukherjee [2]). Despite its relevance, the physics behind CRE formation in polymeric or protein solutions remains less thoroughly explored.

In this work, we focus on protein ring formation in sessile model respiratory droplets. Since the COVID-19 pandemic, this topic has gained significant attention in the disease transmission science community due to its implications for viral infectivity. Remarkably, viral particles (virions) can remain infectious for hours within the dry residue left by evaporated respiratory droplets [33, 29, 35]. This is unexpected, as complete evaporation leads to high salt concentrations which creates, presumably, a harsh chemical environment for virions [40]. One possible explanation to this paradox is that the droplet components—primarily salt and protein [43]—segregate during evaporation. A leading hypothesis, yet to be confirmed [33, 28], is that virions are trapped in protein-rich regions, which protect them from salt-induced damage. Understanding how the protein ring forms may therefore help clarify how viral infectivity depends on relative humidity, H_r .

Some recent studies have addressed this problem qualitatively from a biological perspective. For example, Kong *et al.* [23] and Pan *et al.* [36] analyzed the final residue of evaporated sessile respiratory droplets and found that the final width of the protein ring depends on relative humidity—a behavior that contrasts with predictions for particle-laden droplets. Another intriguing observation is a transition above $H_r = 80\%$: at lower humidity, a protein-rich ring forms near the contact line, while at higher humidity protein is more uniformly distributed, without forming any distinctive structure. Despite these qualitative differences from the classical coffee-ring effect in particle-laden systems, a dedicated theoretical framework for the ring formation in evaporating complex droplets—such as those containing both salt and protein—has not yet been developed.

The first detailed study of the dynamics of deposition rings in particle-laden droplets was carried out by Popov [37], whose framework has since been widely adopted. This model, developed specifically for particle suspensions, relies on two key assumptions. First, the evaporation rate is assumed to be decoupled from the solute transport problem, so it can be readily computed by solving the diffusion-driven vapor transport outside the drop. Then, the evaporation rate thus obtained is used to compute the advective flux in the transport equation. Second, the formation of the deposition ring is driven by this advective flux, which transports particles toward the contact line. As the local particle concentration approaches the maximum packing fraction, further incoming particles cannot penetrate the already-deposited ring and instead accumulate at its inner edge, causing the ring to broaden towards the drop center.

More sophisticated models, such as the one developed by Coombs *et al.* [5] to study the so-called surface capture, build upon these principles. These hypotheses, reasonable for particle-laden suspensions, are crucial for solving the problem analytically as it enables the decoupling of hydrodynamic and transport equations. A recent, very elegant, study by Moore *et al.* [31] introduced the effect of particle diffusion to investigate the early stages of the ring formation using asymptotic techniques. They found that the width of the ring decreases over time as a result of not imposing a maximum packing fraction of particles. This highlights the importance of incorporating a maximum packing fraction in existing models to achieve realistic deposition ring widths.

We refer to these models as constant-activity models (CAM). Although they align well with experiments on particle-laden droplets—for instance, Coombs *et al.* [5] successfully reproduced

the measurements of Li *et al.* [24]—the concept of a particle packing fraction does not naturally extend to complex droplets. Moreover, these theories fail to capture several behaviors observed in polymeric or protein solutions. For example, studies have shown that in evaporating model respiratory droplets, the width of protein rings formed via the coffee-ring effect depends on relative humidity (H_r) [23, 36]. While this dependence may appear intuitive to experimentalists, it contradicts existing reduced models of the coffee-ring effect. In Popov’s framework, H_r only enters through the overall evaporation timescale, implying that the final deposition ring width should be independent of H_r .

In contrast to particle-laden systems, where ring formation is commonly explained by the existence a maximum packing fraction, in polymeric or protein-rich droplets a more natural explanation involves water activity, χ_w . This thermodynamic property quantifies the water vapor pressure at an interface of an aqueous solution relative to that pure water. The water activity takes into account how solutes (like proteins or salts) reduce the evaporation rate. For solutes with a large affinity for water, such as some salts, the water activity can be much smaller than unity, which impacts strongly the evaporation dynamics.

To our knowledge, Salmon *et al.* [39] was the first to theoretically study the surprising qualitative changes in evaporation behavior resulting from the inclusion of water activity. In their work on one-dimensional evaporation of supramolecular mixtures, they showed that evaporation can become nearly insensitive to ambient humidity. This occurs when the water activity drops sharply at high solute concentrations, leading to evaporation rates that vary only weakly with humidity, since the solute concentration at the drying interface becomes nearly independent of it.

Huisman *et al.* [20] experimentally verified this theory by studying the evaporation of polyvinyl alcohol (PVA)–water solutions from open-ended capillaries. They observed that the accumulation of PVA at the evaporating interface forms a polarization layer, which affects both the local diffusivity and the water activity. As a result, the evaporation rate became nearly independent of ambient relative humidity for $H_r \leq 80\%$.

Recently, Thayyil Raju *et al.* [42] investigated the evaporation of glycerol–water solutions from open-ended capillary tubes using both experiments and theoretical modeling. By tracking the height of the upper meniscus, which is not exposed to evaporation, they identified an initial linear decrease in height over time—corresponding to the so-called constant-evaporation-rate stage. As evaporation progressed, glycerol concentration increased at the interface, modifying the water activity χ_w and triggering a transition to the falling-rate stage, where the meniscus velocity followed a power-law decay in time with an exponent of $-1/2$, and a pre-factor that depends on the relative humidity and the initial glycerol concentration.

A number of studies have also focused on the role of water activity in the evaporation and stability of respiratory droplets. For example, Merhi *et al.* [29] combined experimental measurements with theoretical modeling to highlight that incorporating a non-ideal thermodynamic water activity establishes an equilibrium droplet size that becomes independent of relative humidity. Seyfert *et al.* [40] investigated the evaporation of model respiratory droplets on superhydrophobic substrates. They found that at high relative humidity, evaporation halts once the water activity of the solution equals the ambient humidity, i.e., $\chi_w(w_s) = H_r$. Notably, this condition is reached before salt efflorescence occurs (at 20°C for $H_r \geq 0.75$), resulting in droplets that remain stable and liquid indefinitely without fully drying.

These examples illustrate a broader class of systems where evaporation rates are strongly influenced by the composition at the evaporating interface. This effect must be incorporated into any theoretical framework aiming to describe the coffee-ring effect in polymeric or protein-containing droplets. As we will demonstrate, including the dependence of the water activity coefficient, χ_w ,

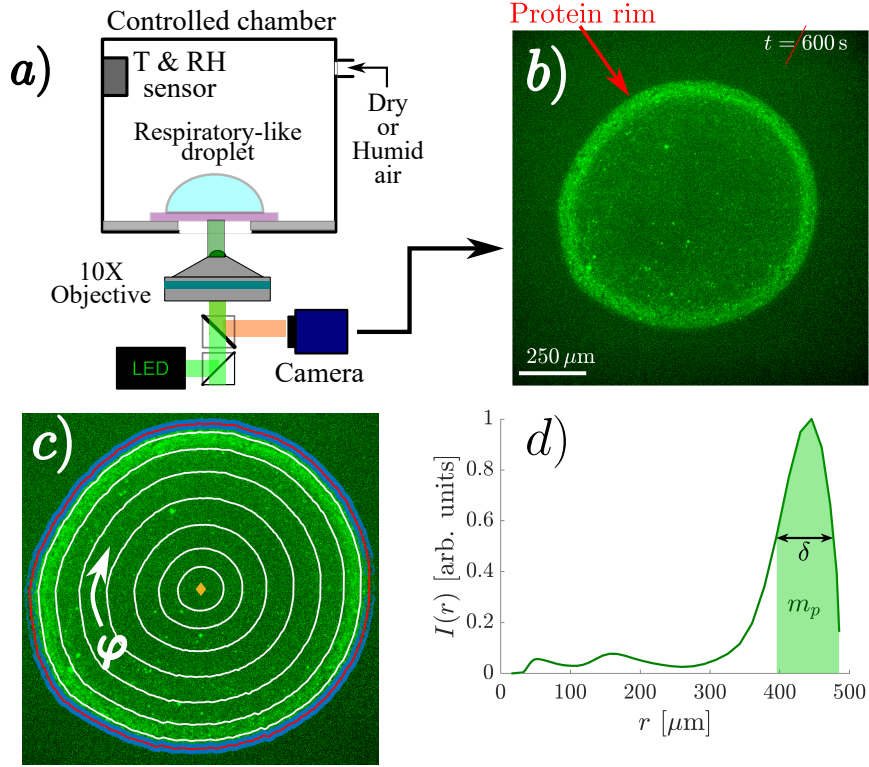


Figure 1: Schematic of the procedure used to obtain the radial intensity profile. a) Time-lapse images of the evaporating droplet are acquired using an epifluorescence microscope inside a humidity-controlled chamber. b) Example of a fluorescence image obtained during evaporation. c) The droplet is segmented into concentric annular regions, and the mean fluorescence intensity is computed for each region. For visualization purposes, fewer regions are shown than were used in the actual analysis. d) From this process, the radial intensity profile is extracted for each image.

on the protein mass fraction, w_p , allows us to explain key experimental observations, such as the relative humidity dependence of the time evolution, and final value, of the ring width.

Our objective is to integrate recent advances from these studies into a comprehensive understanding of coffee-ring formation in complex droplets. To this end, Section 2 presents experimental observations of protein ring formation using fluorescence microscopy. In Section 3, we derive a minimal model that captures the key mechanisms driving the coffee-ring effect in these complex solutions. Section 4 details the formation mechanism of the protein ring, discusses the roles of salt and protein-dependent diffusivity and presents some limitations of the model. Finally, the manuscript concludes with a summary and outlook in Section 5.

2 Experiments

We evaporate artificial saliva droplets following the composition used by Vejerano & Marr [43], namely milliQ water with 9 g L^{-1} of NaCl (Sigma-Aldrich), 3 g L^{-1} of porcine gastric mucin type III (Sigma-Aldrich) and 0.5 g L^{-1} of the pulmonary surfactant 1,2-dihexadecanoyl-sn-glycero-3-phosphocholine. Mucin, the main protein found in respiratory fluids, will be particularly important here, as it is the solute responsible for the ring formation. This composition is commonly used in experimental studies investigating the decay rates of viral infectivity [36].

2.1 Experimental Setup

We deposit sessile model respiratory droplets of initial volume $V_0 = 0.3 \pm 0.1$ μL on μ -Dish 35 mm, high glass-bottom dishes (Ibidi). These micropetri dishes enable high-resolution imaging and do not exhibit autofluorescence. The droplets are evaporated inside a humidity-controlled chamber, at a constant relative humidity (H_r) which varied between 30% and 70% among different experiments. To increase humidity, we introduce humid air into the chamber by recirculating it through a water bottle. For desiccating air, we recirculate it through a separate bottle containing calcium phosphate, a highly hygroscopic salt. This configuration is adapted from Boulogne [3] in order to fit in the reduced space available on a microscope. An scheme of our experimental experimental setup is shown in figure 1.

To assess the spatial distribution of protein, we take advantage of the autofluorescence of mucin, the protein present in model respiratory droplets. Evaporation dynamics were monitored using an inverted widefield fluorescence microscope (Leica DMI8) equipped with a CoolLED pE-4000 illumination system and an Orca-Flash 4.0 sCMOS camera (Hamamatsu). Images were acquired using a $10\times/0.32$ HC PL FLUO objective. Excitation was performed using a 405 nm LED. The microscope was equipped with a quad-band fluorescence filter set (QUA), however, only the channel corresponding to excitation at 405 nm and emission collection at 420–480 nm was used in this study. The exposure time was set to 20 ms per acquisition. To prevent excessive heating of the droplet, we capture images every 5 seconds and verify that the evaporation time matches the theoretical predictions described by Seyfert *et al.* [40].

Due to the axisymmetric nature of the protein rim formation, we focus on the radial intensity profile, defined as:

$$I(r) = \frac{1}{2\pi} \int_0^{2\pi} i(r, \varphi) d\varphi, \quad (1)$$

where $i(r, \varphi)$ is the local intensity in polar coordinates. As the droplet's contact line is not a perfect circle, the radial intensity $I(r)$ is estimated through the following procedure. First, the contact line is extracted from the image and represented as a spline. The centroid is then calculated using $A = \frac{1}{2} \sum_{i=1}^n (x_i y_{i+1} - x_{i+1} y_i)$, $x_c = \frac{1}{6A} \sum_{i=1}^n (x_i + x_{i+1})(x_i y_{i+1} - x_{i+1} y_i)$, and $y_c = \frac{1}{6A} \sum_{i=1}^n (y_i + y_{i+1})(x_i y_{i+1} - x_{i+1} y_i)$, where (x_c, y_c) is the centroid of the spline defined by the ordered vertices (x_i, y_i) . The droplet is then divided into annular regions by constructing inward homothetic splines of the contact line (figure 1c). Within each of these regions, the local intensity is averaged to obtain the corresponding radial intensity. Each homothetic spline is assigned a radius, defined as the mean distance of its points to the centroid of the original contact line. The radial position associated with each annular region is taken as the average of the radii of its inner and outer bounding splines.

In order to obtain the height-averaged concentration profile of mucin, \bar{w}_p from the radial intensity $I(r)$ we follow a similar approach to that employed by Kajiya *et al.* [21]. We assume that the fluorescence intensity follows the relationship

$$I(r) = K \bar{w}_p(r) h(r), \quad (2)$$

where K is a proportionality constant, and $h(r)$ is the height of the drop. To verify the linear relationship between fluorescence intensity, height-averaged protein concentration, and droplet height, we performed a series of calibration experiments. A calibration chamber was constructed using glass slides arranged in an L-shaped geometry, where L denotes the horizontal length of the base and H the vertical height. A thin coverslip was placed on top to enclose the chamber. This configuration creates a wedge-shaped volume of solution with a linearly varying height $h = x(H/L)$

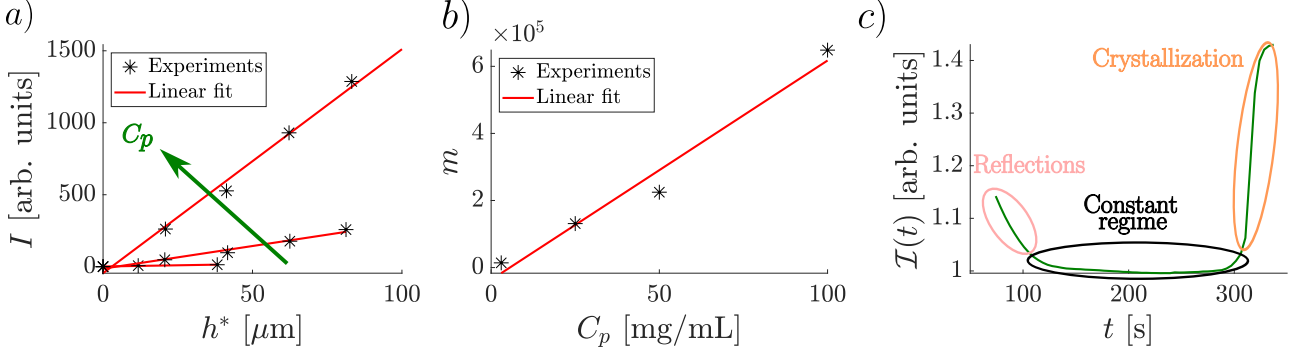


Figure 2: Calibration of fluorescence intensity as a function of droplet height and protein concentration. (a) Fluorescence intensity profiles at different relative heights h^* for varying protein concentrations $C_p = 0.003, 0.025, 0.1$, confirming the linear relationship between intensity and height. (b) Slopes of the fitted lines, m , from (a) demonstrating the linear dependence of fluorescence intensity on protein concentration. (c) Representative time evolution of the total fluorescence intensity, showing distinct regimes during evaporation. All quantitative analyses presented throughout this article are based on data from the constant-intensity regime.

where x is the horizontal direction. By translating the microscope objective along this direction, we can access fluorescence signals at known and controllable sample heights, enabling calibration of the fluorescence response as a function of height. We acquired fluorescence images of protein solutions with $\bar{w}_p = 0.003, 0.025, 0.05, 0.1$. Higher protein concentrations ($\bar{w}_p > 0.1$) could not be dissolved in water and salt to produce a uniform mixture. For each concentration, we verified the linear relationship between fluorescence intensity and solution height (see figure 2a). To test the dependence on \bar{w}_p , we found that the slopes of the fitted lines relating intensity to height scale linearly with the height-averaged protein concentration (see figure 2b). As a consequence of this linearity, from equation 2, the total amount of light intensity $\mathcal{I}(t)$ follows

$$\mathcal{I}(t) = \int_0^{R_c} 2\pi r I(r, t) dr = \int_0^{R_c} 2\pi r K \bar{w}_p(r, t) h(r, t) dr = K M_p, \quad (3)$$

where R_c is the contact radius and M_p is the total amount of protein in the droplet, that remains constant throughout the experiment. At the beginning of the evaporation process, the relatively high contact angle (approximately 60°) leads to optical reflections near the contact line, which artificially increase the measured fluorescence intensity $\mathcal{I}(t)$. To avoid this artifact, our analysis begins only after these reflections disappear and the system enters a regime in which $\mathcal{I}(t)$ remains constant. Within this regime, the intensity varies by less than 1% throughout each experiment. Following this stable period, droplets exposed to low and medium relative humidity eventually crystallize, causing a sharp increase in $\mathcal{I}(t)$. Our analysis is therefore restricted to the temporal window between the disappearance of initial reflections and the onset of crystallization (see figure 2 c).

It should be noted that although both mucin and salt crystals were visualized using fluorescence microscopy with excitation at 405 nm and emission detection between 420–480 nm, only mucin exhibits intrinsic autofluorescence in this spectral window. Inorganic salt crystals do not emit fluorescence under these conditions. The signal observed from salt crystals is therefore attributed primarily to light scattering rather than true fluorescence emission. Additionally, it is possible that mucin molecules become adsorbed or deposited onto the surfaces of salt crystals during droplet

evaporation, resulting in localized fluorescence signals that spatially coincide with the crystal structures. A detailed investigation of this complex interplay is beyond the scope of the present work, but it constitutes an interesting avenue for future research.

From fluorescence experiments, we obtain the radial intensity as $I(r) = K \bar{w}_p h$. However, due to spatial constraints within the microscope setup, it is not possible to image the droplet from the side during fluorescence experiments. As a result, we cannot directly measure the interface height profile $h(r, t)$. To circumvent this limitation, we work with the height-integrated protein fraction $\phi_p = h \bar{w}_p$ for analyzing the spatial distribution of protein.

2.2 Experimental Results

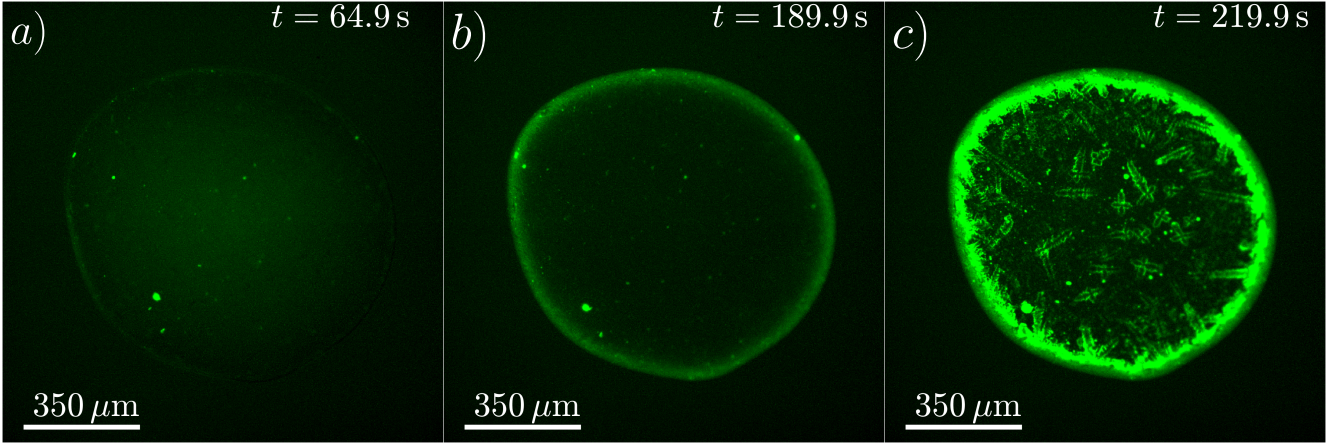


Figure 3: Fluorescence images showing the initial homogeneous distribution of protein, the formation of a peripheral protein ring, and final crystallization.

As evaporation progresses, protein begins to accumulate near the contact line, creating a protein ring. We observe that this protein ring increases in both intensity and width over time. From a practical perspective, in model respiratory droplets, a relevant feature of the protein ring is its width, δ . The width of the protein ring has been linked to the low decay rates of virions' infectivity in dry residues of model respiratory droplets Huang *et al.* [19]. Protein is expected to shroud virions, slowing their loss of infectivity [45]. This implies that a wider protein-rich region could help virions to remain infective for a longer period.

We define the width of the coffee-ring, δ , as that of the peak at half prominence (figure 1 d). We adopt this definition because measuring the peak width at half height, as done in analytical theories like those of Popov [37] and Moore *et al.* [31], is experimentally challenging for high relative humidity. In these cases, the height of the peak does not allow for easy identification of the intersection at half height in the inner part of the protein ring.

The most striking phenomena we found in experiments is that the width δ follow different dynamics for different relative humidity (see figure 4 d) and that the maximum height-integrated protein fraction ϕ_p of the protein ring decreases as the relative humidity increases (see figure 4 f). As explained on the introduction in constant-activity models the width of the coffee ring has been found to follow the same scaling law across all values of the relative humidity. However, as shown in figure 4 d, this behavior does not hold for protein ring formation in sessile model respiratory droplets. In this figure we show the time evolution of the rim width for drops evaporating at different humidity, with the time scaled with the diffusive timescale, $t_d = \rho R_c^2 / D_{\text{vap}} C_s (1 - H_r)$.

This timescale is computed with the density of water, ρ , the contact radius, R_c , the diffusivity of water vapour on air, D_{vap} , the saturation concentration of water vapour in air, C_s and the ambient relative humidity, H_r . Because of experimental limitations in determining the exact onset of deposition, the initial time of each experiment carries some uncertainty. To account for this, we reset the origin of the temporal axis by introducing $t_{10\%}$, defined as the time at which the protein mass accumulated in the ring reaches 10% of the total protein mass in the droplet.

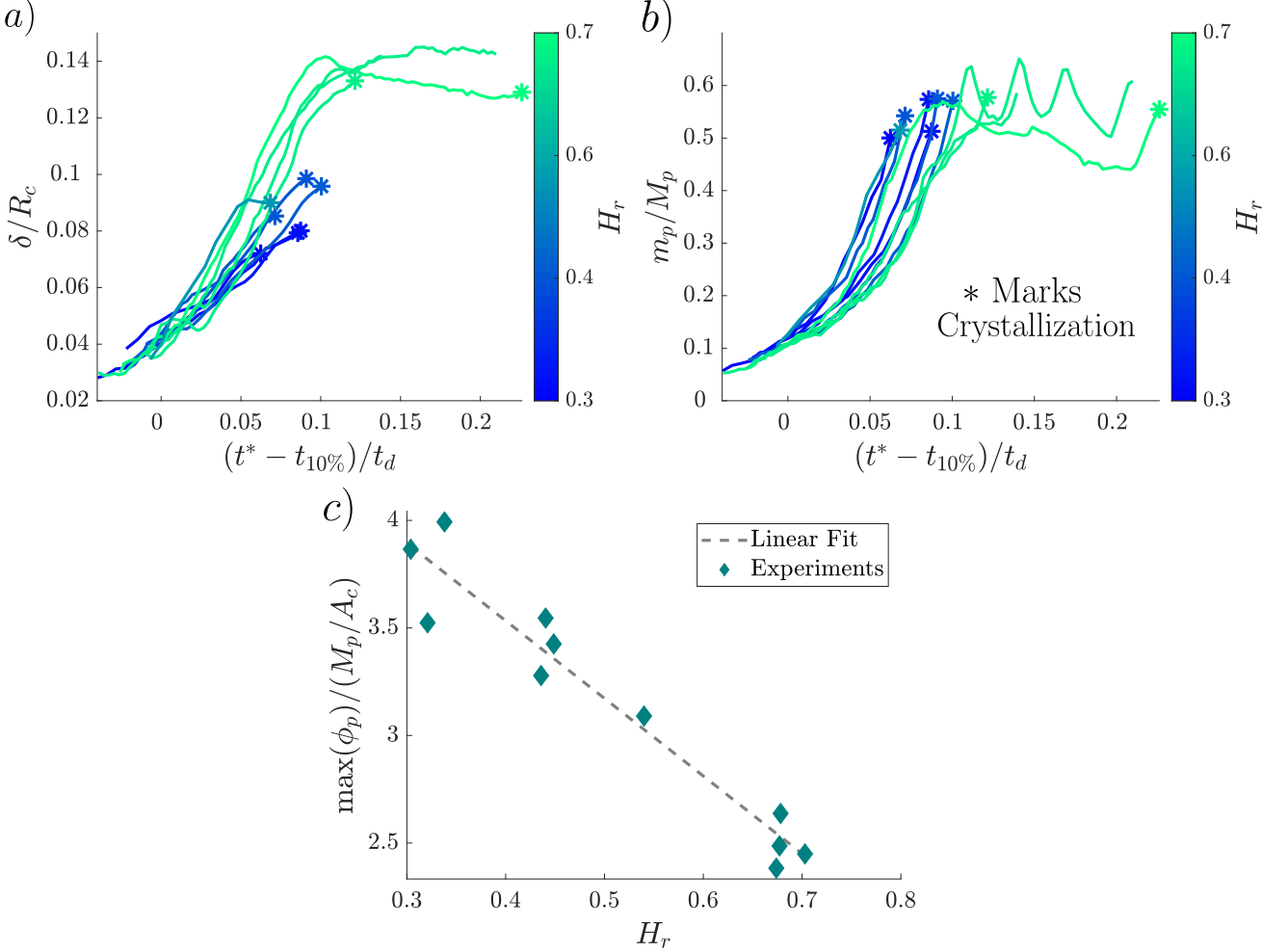


Figure 4: Experimental results. (a) Temporal evolution of the ring width, δ . (b) Mass of protein, m_p , in the ring normalized by the total protein mass in the droplet, M_p , as a function of time. (c) Dependence of the maximum height-integrated protein fraction, normalized by the total protein mass in the droplet divided by the contact area A_c , with the relative humidity.

We can see how, at low and medium relative humidity, the growth of the rim width, δ , is slower than at high relative humidity when time is non-dimensionalized using the diffusive timescale. We must insist that the rim widths predicted by Popov [37] collapse on a single curve for all H_r when the time is non-dimensionalized with t_d . In more sophisticated theories, such as those of Coombs *et al.* [5] and Moore *et al.* [31], the temporal evolution curves of the ring width exhibit an offset that depends on the Péclet number (Pe), while their slope remains unchanged. In contrast, our experimental results show that the slope increases with higher relative humidity (H_r). This phenomenon, which cannot be explained by existing theories of the coffee-ring effect, can be understood by considering the dependence of the water activity on both salt and protein mass

fractions (see Section 4 for a detailed discussion).

3 Mathematical model

In this section, we present a minimal theoretical model aimed at capturing the essential dynamics of the coffee-ring effect (CRE) in polymeric or protein solutions, as observed in our experiments (see Section 2). The goal is not to achieve a one-to-one quantitative comparison with the experimental results, but rather to use the experimental observations as motivation to explore physical mechanisms that are not adequately explained by existing theoretical models.

As discussed in the Introduction, most existing models of the coffee-ring effect (CRE) have been developed in the context of particle-laden droplets. To reproduce the formation of a realistic ring width, these models typically rely on the assumption of a maximum packing fraction w_{pc} [37, 22, 5]. This assumption leads to a separation of the droplet into two distinct regions: one where the local particle concentration is exactly w_{pc} , forming the dense particle ring, and another where the concentration remains below w_{pc} , corresponding to a dilute region. This framework also allows for a decoupling of the hydrodynamic problem from the transport problem, significantly simplifying the analysis. While this approach may be appropriate for suspensions of particles, it becomes less adequate when applied to polymeric or protein solutions as, in such systems, there is no natural extension of a maximum packing fraction. As a result, the use of w_{pc} in this context is somewhat arbitrary and does not accurately capture the underlying physics of polymer or protein ring formation.

In contrast, here we adopt a different approach in which the entire droplet is treated as a single continuous phase. Consequently, the equations we derive are valid throughout the entire droplet and remain applicable at all times during the evaporation process.

As it has been shown [28], the flow pattern in respiratory droplets can be recirculatory due to natural convection. In other contexts, recirculation may also arise from Marangoni stresses [27, 9]. For a detailed two-dimensional model that accounts for these phenomena, we refer the interested reader to Diddens *et al.* [11], Dekker *et al.* [9], Martínez-Puig *et al.* [28]. In the present work, however, our goal is to develop a minimal model that explain the mechanism behind the coffee ring effect in polymeric or protein solutions. To that end, we adopt the lubrication approximation and derive a one-dimensional model to describe the hydrodynamics and solute transport within the droplet.

3.1 Flow problem

In order to apply the lubrication approximation, we assume that $\epsilon = h_0/R_c \ll 1$, where h_0 is the initial height of the droplet at $r = 0$. In this formulation, we neglect the effect of gravity, which corresponds to assuming a small Bond number Bo , as is typically valid for droplets with radii smaller than a millimeter. Since we work with height-averaged radial velocity \bar{u}_r in the transport equation, we also neglect buoyancy forces in the hydrodynamic equations, as they are of order ϵ^2 . Although Marangoni effects can be incorporated within the lubrication framework, previous studies [12, 28], have shown that surface tension gradients are negligible in protein-laden mixtures, due to the accumulation and jamming of proteins at the interface. We further assume that the flow is axisymmetric so we have in cylindrical coordinates

$$\frac{\partial h^*}{\partial t^*} + \frac{1}{r^*} \frac{\partial}{\partial r^*} (r^* h^* \bar{u}_r^*) = -\frac{J^*}{\rho^*}, \quad \bar{u}_r^* = -\frac{h^{*2}}{3\mu^*} \frac{\partial p^*}{\partial r^*}, \quad p^* = p_{atm}^* - \frac{\gamma^*}{r^*} \frac{\partial}{\partial r^*} \left(r^* \frac{\partial h^*}{\partial r^*} \right), \quad (4)$$

where h is the height of the droplet, t is the time, r is the radial coordinate, J is the local evaporation rate, ρ is the density of the suspension, \bar{u}_r is the height-averaged radial velocity, μ is the suspension viscosity, p is the pressure, p_{atm} is the atmospheric pressure and γ is the surface tension of the suspension. The superscript $*$ denotes dimensional variables. Equation 4 is subject to symmetry boundary conditions at the symmetry axis

$$\frac{\partial h^*}{\partial r^*} = Q^* = 0 \text{ at } r^* = 0,$$

where $Q^* = r^* h^* \bar{u}_r^*$ is the local flow rate. At the contact line there is no flux and the height is zero

$$h^* = Q^* = 0 \text{ at } r^* = R_c.$$

As we have neglected the influence of gravity in the droplet shape the initial condition is that of a spherical cap

$$h^* = \frac{h_0}{R_c^2} (R_c^2 - r^{*2}) \text{ at } t^* = 0.$$

3.2 Solute transport problem

To remain consistent in the derivation of the solute transport equations we assume again that $\epsilon \ll 1$. This approximation allows the simplification of the model. The characteristic vertical diffusive timescale in a droplet is given by $t_{dz} = h_0^2/D_p$, where D_p is the solute diffusivity. The corresponding vertical evaporative timescale is $t_{evz} = h_0/(J_c/\rho)$, where $J_c = D_{vap}C_s/R_c$ is a characteristic evaporation rate, with D_{vap} the vapor diffusivity in air, and C_s the saturation concentration of water vapor. For a water-based droplet evaporating under ambient conditions, we take $D_{vap} \sim 10^{-5} \text{ m}^2/\text{s}$, $C_s \sim 0.015 \text{ kg/m}^3$, and $\rho \sim 10^3 \text{ kg/m}^3$, yielding $t_{dz}/t_{evz} \sim 10^{-10} \epsilon/D_p$ where $\epsilon = h_0/R_c \ll 1$ is the aspect ratio of the droplet. This scaling implies that, for solutes with diffusivity $D_p \gtrsim 10^{-10} \text{ m}^2/\text{s}$, and provided that $\epsilon \ll 1$, vertical diffusion is much faster than vertical advection due to evaporation. Therefore, we can reasonably assume that the solute concentration is vertically homogeneous at all times. This observation motivates the use of a height averaged advection–diffusion equation to describe the transport of solute within the droplet

$$\frac{\partial}{\partial t^*} (h^* \bar{w}_p) + \frac{1}{r^*} \frac{\partial}{\partial r^*} (r^* h^* \bar{u}_r^* \bar{w}_p) = \frac{1}{r^*} \frac{\partial}{\partial r^*} \left(D_p^* r^* h^* \frac{\partial \bar{w}_p}{\partial r^*} \right). \quad (5)$$

This equation is subjected to symmetry conditions at the symmetry axis

$$\frac{\partial \bar{w}_p}{\partial r^*} = 0 \text{ at } r^* = 0.$$

As the solute is non-volatile we impose a no-flux condition at the contact line

$$r^* h^* \bar{u}_r^* \bar{w}_p - D_p^* r^* h^* \frac{\partial \bar{w}_p}{\partial r^*} = 0 \text{ at } r^* = R_c.$$

We further assume that the solute is initially well-mixed so the initial condition is

$$\bar{w}_p = w_{p0} \text{ at } t^* = 0,$$

where w_{p0} is constant.

3.3 Evaporation Rate

Up to this point, if viscosity and diffusivity are assumed to be constant and independent of solute concentration, the hydrodynamic problem is decoupled from the transport of solute. However, this decoupling breaks down when we account for the fact that evaporation itself depends on local solute concentration. It is well established that the water activity—and therefore the local evaporation rate—is a function of solute concentration for many polymers and proteins. This introduces a critical feedback mechanism: the solute concentration affects the evaporation rate (Salmon *et al.* [39], Thayyil Raju *et al.* [42]), which in turn modifies the flow field and solute transport. In the following we describe how to account for this coupling through the evaporation rate.

The large evaporation timescale, $t_{\text{ev}} \sim 10^2 \text{ s}$, compared to the characteristic diffusive timescale of water vapor in the gas phase, $t_{d_G} = R_c^2/D_{\text{vap}} \sim 10^{-1} \text{ s}$, justifies the assumption of quasi-steady diffusion of water vapor in the surrounding air

$$\nabla^2 C_{\text{vap}}^* = 0. \quad (6)$$

Provided that the droplet is thin, the Dirichlet condition at the droplet-air interface is imposed at $z^* = 0$

$$C_{\text{vap}}^* = C_s \chi_w \text{ at } z^* = 0, \quad 0 < r^* < R_c.$$

This condition arises from the assumption of thermodynamic equilibrium between the droplet and the surrounding vapor phase. The water activity, χ_w , accounts for the reduction in the equilibrium vapor concentration at the droplet interface due to the presence of solutes, relative to that of a pure water droplet. This condition needs to be complemented with the symmetry condition

$$\frac{\partial C_{\text{vap}}^*}{\partial r^*} = 0 \text{ at } r^* = 0,$$

the no-flux condition on the substrate outside the droplet

$$\frac{\partial C_{\text{vap}}^*}{\partial z^*} = 0 \text{ at } r^* > R_c,$$

and the far-field condition

$$C_{\text{vap}}^* = C_s H_r \text{ at } r^* \rightarrow \infty, \quad z^* \rightarrow \infty.$$

Formally, on a thin droplet where the water vapour transport is diffusive, the evaporation rate is

$$J^* = -D_{\text{vap}}^* \frac{\partial C_{\text{vap}}^*}{\partial z^*} \text{ at } z^* = 0, \quad 0 < r^* < R_c.$$

This problem can be solved analytically, as shown by Popov [37], for the case of a constant Dirichlet boundary condition at the air–water interface, i.e., when the water activity χ_w remains constant. However, to capture the rich phenomenology of the evaporation dynamics of polymeric or protein solutions, the water activity must be treated as concentration-dependent, $\chi_w(\bar{w}_p)$, and therefore varies along the droplet radius. This class of problems is classical in potential theory [6]. One approach is to apply the Hankel transform, which reduces the problem to a dual integral equation [34], although this method is algebraically cumbersome. A more elegant and tractable solution, based on techniques from complex analysis, was presented by Green & Zerna [17], yielding the following expression for the evaporation rate:

$$J^* = -D_{vap}C_s \frac{1}{r^*} \frac{\partial}{\partial r^*} \int_{r^*}^{R_c} \frac{r' g(r') dr'}{\sqrt{r'^2 - r^{*2}}} \quad (7)$$

where

$$g(r') = \frac{2}{\pi} \frac{d}{dr'} \int_0^{r'} \frac{r (\chi_w(r) - H_r) dr}{\sqrt{r'^2 - r^2}}. \quad (8)$$

Notably, this formulation recovers the analytical solution of Popov [37] as a special case when χ_w is constant. Solving these integrals analytically for a non-constant χ_w remains far from trivial. Fu *et al.* [14] derived an explicit expression for the auxiliary function $g(r')$ under the assumption that $\chi_w(r)$ can be represented as a polynomial. This allows a symbolic computation of the evaporation rate J^* using mathematical software. However, when strong spatial gradients in χ_w are present, polynomial approximations tend to introduce spurious oscillations in the evaporation rate. To overcome this limitation, we adopt a semi-analytical approach that is robust regardless of the smoothness of χ_w . Specifically, we represent χ_w using cubic splines, which permits an analytical solution for $g(r')$, followed by a numerical integration to evaluate J^* . The strength of this method lies in the ability of cubic splines to approximate arbitrary continuous functions without inducing artificial oscillations. Technical details of the spline-based implementation are provided in Appendix 5.

3.4 Non-dimensionalization

The characteristic scales of the problem are those induced by evaporation. Thus the characteristic velocity is given by evaporation as $v_c = J_c^*/\rho^*\epsilon$, where $J_c^* = D_{vap}C_s(1 - H_r)/R_c$. Based on this scale, we introduce the following dimensionless variables:

$$\begin{aligned} r &= \frac{r^*}{R_c^*}, & z &= \frac{z^*}{\epsilon R_c^*}, & \bar{u}_r &= \frac{\epsilon \rho^* \bar{u}_r^*}{J_c^*}, & t &= \frac{J_c^* t^*}{\epsilon \rho^* R_c^*}, \\ h &= \frac{h^*}{\epsilon R_c^*}, & p &= \frac{(p^* - p_{atm}) \rho^* R_c^* \epsilon^3}{\mu_w^* J_c^*}, & \mu &= \frac{\mu^*}{\mu_w^*}, & J &= \frac{J^*}{J_c^*}. \end{aligned} \quad (9)$$

Notice that, a priori, the viscosity varies with protein concentration. Therefore, we choose the viscosity of pure water, μ_w^* , as the characteristic viscosity for non-dimensionalization. Introducing this non-dimensional variables the flow problem becomes

$$\frac{\partial h}{\partial t} + \frac{1}{r} \frac{\partial}{\partial r} (r h \bar{u}_r) = -J, \quad \bar{u}_r = -\frac{h}{3\mu Ca} \frac{\partial p}{\partial r}, \quad p = -\frac{1}{r} \frac{\partial}{\partial r} \left(r \frac{\partial h}{\partial r} \right), \quad (10)$$

subjected to symmetry boundary conditions at the symmetry axis

$$\frac{\partial h}{\partial r} = Q = 0 \text{ at } r = 0,$$

and no-flux and zero-height condition at the contact line

$$h = Q = 0 \text{ at } r = 1.$$

with the initial condition

$$h = 1 - r^2 \text{ at } t = 0.$$

Here $Ca = J_c^* \mu_w^* / \gamma^* \rho^* \epsilon^4$ is the capillary number. The Capillary number is typically small for water-based droplets evaporating under ambient conditions. In our experiments, for instance, we estimate $Ca \sim 10^{-6} \ll 1$, indicating that surface tension dominates over viscous forces, and the droplet interface is expected to remain close to a spherical cap. However, as we will discuss in subsequent sections, the viscosity of protein solutions can increase significantly with concentration. In such cases, the product μCa becomes of order unity or larger, suggesting that viscous effects could deform the interface away from the spherical cap shape.

Introducing this non-dimensional variables the solute problem becomes

$$\frac{\partial}{\partial t} (h \bar{w}_p) + \frac{1}{r} \frac{\partial}{\partial r} (r h \bar{u}_r \bar{w}_p) = \frac{1}{Pe} \frac{1}{r} \frac{\partial}{\partial r} \left(D_p r h \frac{\partial \bar{w}_p}{\partial r} \right), \quad (11)$$

where we have used the diffusivity of the protein in a very dilute solution, denoted D_{p0}^* , as the characteristic diffusivity for non-dimensionalization. Accordingly, the dimensionless diffusivity is defined as $D_p = D_p^* / D_{p0}^*$, where D_p^* is the local protein diffusivity. This equation is subjected to symmetry conditions at the symmetry axis

$$\frac{\partial \bar{w}_p}{\partial r} = 0 \text{ at } r = 0,$$

and no-flux condition at the contact line

$$h \left(\bar{u}_r \bar{w}_p - \frac{1}{Pe} \frac{\partial \bar{w}_p}{\partial r} \right) = 0 \text{ at } r = 1,$$

with initial condition

$$\bar{w}_p = w_{p0} \text{ at } t = 0.$$

The Péclet number is defined as $Pe = J_c^* R_c^* / \rho^* D_{p0}^* \epsilon$. The formation of a protein rim requires $Pe \gg 1$, which ensures that the advective mass flux is strong enough to overcome the opposing diffusive flux.

Finally the non-dimensional evaporation rate can be computed by

$$J = -\frac{1}{r} \frac{\partial}{\partial r} \int_r^1 \frac{r' g(r') dr'}{\sqrt{r'^2 - r^2}} \quad (12)$$

where

$$g(r') = \frac{2}{\pi} \frac{d}{dr'} \int_0^{r'} \frac{r (\chi_w(r) - H_r) dr}{\sqrt{r'^2 - r^2}}. \quad (13)$$

For details of the numerical scheme used to solve this dimensionless model, the interested reader is referred to Appendix 5.

3.5 Water activity and material properties

Water activity is known to depend on both protein and salt mass fractions [47, 30]. However, to the best of our knowledge, the combined effect of protein and salt on water activity has not been studied systematically in the literature. To obtain a realistic representation of the water activity $\chi_w(\bar{w}_p, w_s)$, we combine empirical measurements of water activity in the presence of protein,

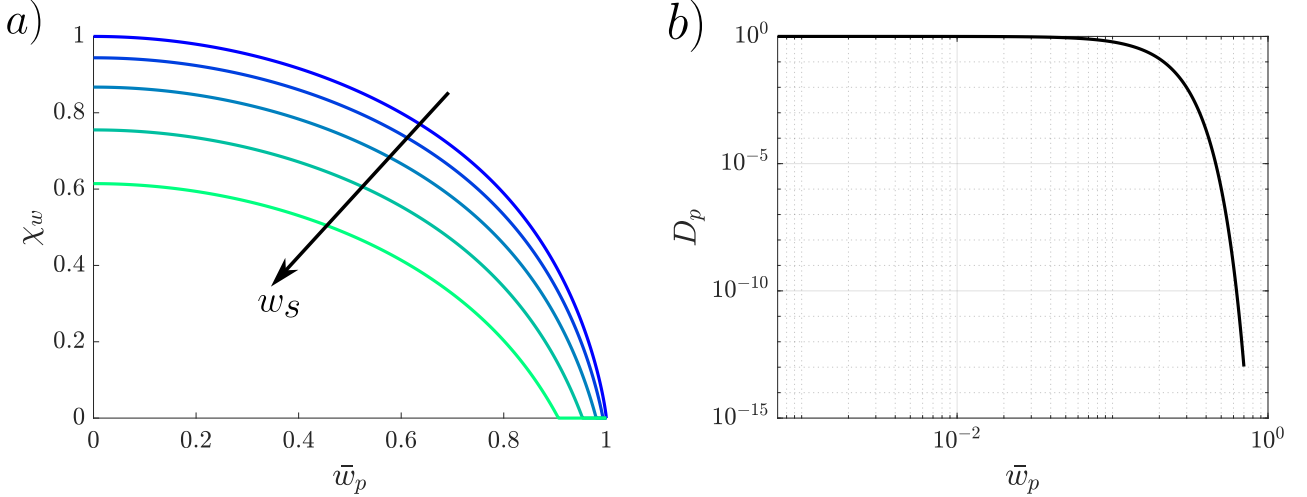


Figure 5: Material and thermodynamical properties used in the model. (a) Water activity as a function of protein mass fraction for different salt mass fractions $w_s = 0, 0.09, 0.18, 0.26, 0.35$. Increasing salt concentration shifts the water activity curves downward. (b) Evolution of protein diffusivity as a function of protein concentration, display on a logarithmic scale.

$\chi_w^p(\bar{w}_p)$ [47], with those corresponding to salt concentration, $\chi_w^s(w_s)$ [30]. Then the water activity will read

$$\chi_w(\bar{w}_p, w_s) = \chi_w^p(\bar{w}_p) + \chi_w^s(w_s) - 1,$$

here w_s is the salt mass fraction on the solution. We do not include an explicit transport equation for salt in our formulation. This simplification is justified by the high salt diffusivity, $D_s^* = 10^{-9} \text{ m}^2/\text{s}$, which yields Péclet numbers on the order of $Pe_s \sim 1$. Thus, we assume that the salt remains well mixed throughout the droplet at all times [40, 28]. Given the initial salt mass fraction w_{s0} and the initial droplet volume V_0 , the total salt mass is $M_s = w_{s0} V_0$. The droplet volume at any time is $V(t) = 2\pi \int_0^1 r h(r, t) dr$, which allows us to compute the instantaneous salt mass fraction as $w_s(t) = M_s/V(t)$. We have assumed that the solution density remains constant.

The difference in diffusivity between salt and protein is crucial in the formation of deposition patterns. The relatively low diffusivity of proteins enables the development of strong spatial concentration gradients near the contact line, which in turn makes the formation of a protein-rich ring possible. In contrast, the high diffusivity of salt ensures that it remains well mixed throughout the droplet, preventing the buildup of localized concentration gradients. This distinction is clearly reflected in the experimental salt deposition patterns (see figure 4). Unlike the protein, which accumulates locally to form a concentrated ring near the contact line, salt crystals are observed throughout the entire droplet footprint. For a more thorough discussion and modeling of salt transport, we refer the interested reader to Martínez-Puig *et al.* [28].

From the perspective of water activity, this has an important implication: the effect of salt on water activity is inherently global, as the salt concentration is approximately uniform across the entire interface. In contrast, the contribution of protein to water activity is local, affecting only regions where the protein mass fraction becomes sufficiently high. This localized influence can lead to spatially heterogeneous evaporation rates, which drive the advective transport necessary for ring formation. In figure 5 a) we show the dependence of water activity on both protein and salt mass fractions.

We did not find experimental measurements of mucin diffusivity in the literature. Therefore, we use a diffusivity similar to that proposed by Salmon *et al.* [39] for complex fluids. In our case, we use

$$\log_{10} D_p^*(\bar{w}_p) = a_4 \bar{w}_p^4 + a_3 \bar{w}_p^3 + a_2 \bar{w}_p^2 + a_1 \bar{w}_p + a_0, \quad (14)$$

where $[a_4; a_3; a_2; a_1; a_0] = [-14.65; 5; -22.97; 0.12; -11]$ (see figure 5 b).

4 Model results and comparison with experiments

4.1 Formation mechanism of the protein ring

To describe the dynamics of a nascent coffee ring, Moore *et al.* [31] presented a model similar in structure to the one developed here, but in which the hydrodynamics and solute transport are decoupled. In the asymptotic limits $\text{Ca} \ll 1$ and $\text{Pe} \gg 1$, they showed that the protein ring sharpens and ultimately converges to a singular line as evaporation progresses. This naturally raises the question: how can a finite ring width emerge without imposing an artificial constraint such as a maximum packing fraction, as proposed by constant-activity models?

In our model, the growth of the ring width is a natural consequence of the coupling between solute transport and hydrodynamics through an activity-dependent evaporation rate. In order to understand the proposed minimal mechanism behind the formation and widening of the ring, let us assume for now that the physical properties are constant and that there is no salt in the mixture, so we let $\mu = D_p = 1$ and $w_{s0} = 0$. In figure 6 we show the temporal evolution of the evaporation rate J , the water activity χ_w , the advective flux $J_{\text{adv}} = \bar{u}_r h w_p$, and the height-integrated protein fraction ϕ_p , for a simulation with $\text{Ca} = 10^{-4}$, $\text{Pe} = 13.2$, $w_{p0} = 3 \times 10^{-3}$, and $H_r = 0.7$.

At early stages, when the water activity $\chi_w \approx 1$ everywhere, the evaporation rate presents a sharp maximum near the contact line, driving a strong advective flux of protein towards the edge which, in turn, leads to the local accumulation of solute. If the evaporation rate does not depend on the solute concentration, then it diverges to infinity at the contact line at all times. However, this situation is modified when we let the water activity be a decreasing function of the solute concentration. As a result of the large evaporation rate near the contact line, water is quickly depleted there, which diminishes the evaporation rate (figure 6a) and regularizes the singularity. Also, the maximum evaporation rate shifts radially inwards, away from the contact line. It is worth mentioning here that, as has been previously discussed for the formation of the coffee ring in particle-laden droplets, the presence of a singularity in the evaporation rate is not essential to create a coffee ring [4, 13], as we also show here.

In the limit of small capillary number, the dominant surface tension forces impose a spherical-cap interface at all times. Mass conservation then uniquely determines the flow rate Q for $\partial h / \partial t$ to be compatible with a spherical-cap interface. In particular, it dictates that the maximum flow rate is going to be close to the location where the evaporation rate peaks.

In fact, in the case $\mu = 1$, the water flux demanded by the evaporation peak can be as strong as to reverse the flow in the region between the maximum evaporation rate and the contact line, which corresponds to the protein rim, figure 6b. Although this effect, which we dub *protein rim squeezing*, is regularized if we let the viscosity grow large enough with the protein concentration (see section 4.3.1 for a detailed discussion). In any case, even if the flow rate never becomes negative, the strong advective flux directed to the evaporation rate peak transports protein mostly towards

the inner region of the ring, promoting its widening. In fact, in figure 6c we see how the protein ring extends from the contact line to the location of maximum of the evaporation rate.

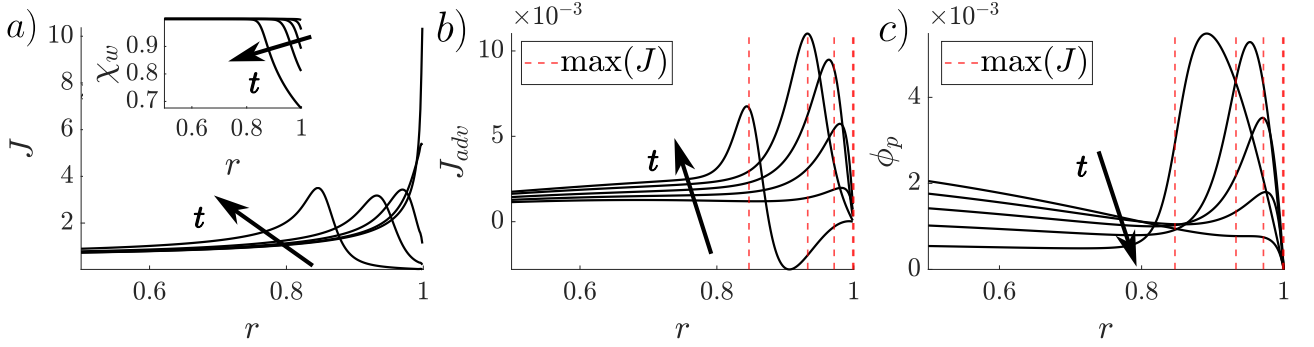


Figure 6: Mechanism of ring formation during droplet evaporation. (a) Temporal evolution of the evaporation rate, with the inset showing the corresponding evolution of water activity. (b) Temporal evolution of the advective flux and the maximum evaporation rate. (c) Temporal evolution of the height-integrated protein fraction together with the maximum evaporation rate. Data are shown at non-dimensional times ($t = (0.1, 0.3, 0.5, 0.7, 0.9)$), with parameters $Ca = 10^{-4}$, $Pe = 13.2$, $w_{p0} = 3 \cdot 10^{-3}$ and $H_r = 0.7$.

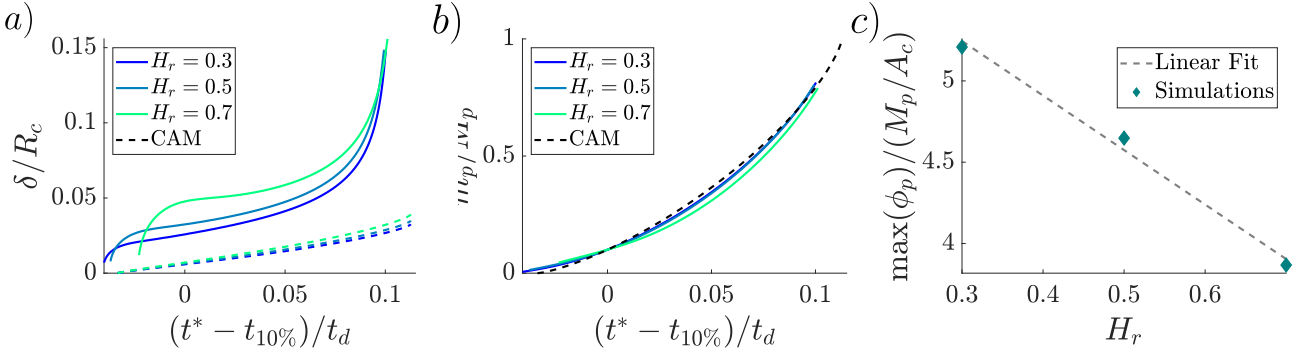


Figure 7: Evolution of the ring morphology during droplet evaporation. (a) Temporal evolution of the ring width. (b) Temporal evolution of the protein mass in the ring, normalized by the total protein mass in the droplet. (c) Maximum height-integrated protein mass fraction, normalized by the total protein mass in the droplet divided by the contact area A_c , as a function of relative humidity. The parameters used are $Ca = 10^{-4}$, $Pe = 43.3(1 - H_r)$, initial protein mass fraction $w_{p0} = 3 \cdot 10^{-3}$, and relative humidity values $H_r = 0.3, 0.5, 0.7$.

In figures 7a and 7b we show the model results, which portrait the time evolution of the rim width and mass for three different values of the relative humidity. We use the same parameters as in figure 6, considering relative humidity values of $H_r = 0.3, 0.5$, and 0.7 . Additionally, we present the evolution of the final maximum of the height-integrated protein fraction ϕ_p as a function of the relative humidity. Despite its simplicity, our minimal model—where salt is neglected and material properties are constant—qualitatively reproduces the most salient features observed in experiments: the dependence of the final rim width with the relative humidity, the insensitivity of rim mass evolution to the relative humidity, and the decreasing trend of the maximum height-integrated protein fraction with the relative humidity.

We can explain why, containing nearly the same mass, the rim width grows monotonically with the humidity. The relative humidity appears in the problem through the difference $\chi_w - H_r$ (Equations (7)-(8)). As this factor approaches zero near the contact line (becoming instantaneously zero there at $t = 0^+$), the peak of maximum evaporation rate smoothens up, and the location of maximum evaporation shifts inward. This transition occurs earlier the higher the relative humidity, because less protein needs to accumulate near the contact line to satisfy the condition $\chi_w(w_p) - H_r \ll 1$. As a result, the ring width increases more rapidly the higher the humidity. Then, since the ring mass is rather insensitive to the humidity, the maximum height-integrated protein concentration must therefore decrease.

To compare the measured ring width with the theoretical prediction of constant-activity models (CAM), we will use the work of Popov [37]. We need to impose a maximum protein concentration, equivalent to a maximum particle packing fraction. Nevertheless, CAM predict ring widths more than three times smaller than those obtained with our model (figure 7a). This discrepancy can be attributed to two main factors. First, the protein concentration within the rim is not homogeneous. Second, the maximum protein concentration in the ring evolves over time rather than remaining constant. Since the protein concentration in our model remains, for most of the time and across most of the ring, below the maximum concentration reached during the entire evaporation process, the rim must be thicker than in Popov’s description.

The ring mass, however, compares reasonably well with the theoretical prediction of Popov [37], originally derived by Deegan *et al.* [8]. In the absence of diffusion, the ring mass is determined by the advective flux driven by evaporation, implying that it should correlate with the total mass of water lost from the droplet. Although the maximum of the evaporation rate is shifted toward the inner region of the ring—leading to a thickening of the deposit—the overall ring mass remains close to Popov’s prediction, provided that the total evaporated mass is similar. As shown in figure 8(a), the droplet volume decreases almost linearly with time, in agreement with Popov’s theory. The same reasoning also explains why the evolution of protein mass in the ring shows little dependence on relative humidity: since the volume evolution is nearly unaffected by the humidity when represented against the non-dimensional time, the total advective flux required to replenish water losses near the contact line is also similar.

The influence of the humidity in the protein ring evolution depends on the functional form of the water activity $\chi_w^p(\bar{w}_p)$. For example, if an ideal binary mixture is assumed, such that $\chi_w^p(\bar{w}_p) \sim 1 - w_p$ [29], then the relationship between humidity and rim formation becomes nearly linear. However, this is not the case in more complex solutions, which depart from ideal behavior and account for non-equilibrium effects. In our model, based on a non-ideal $\chi_w^p(\bar{w}_p)$, the difference in behavior between medium and high relative humidity is more pronounced than that between low and medium. This is because the critical concentration w_{p_c} satisfying $\chi_w(w_{p_c}) = H_r$ is similar for low and medium humidity, but differs significantly for high humidity (see appendix 5 for a detailed discussion on different water activities).

Although our minimal model qualitatively captures the main trends observed in the experiments, additional complexity is required to fully explain the differences between figure 7 and figure 4. In the following subsection, we analyze the combined influence of salt and non-constant diffusivity.

4.2 Role of salt and non-constant diffusivity.

In our experiments, we observe that droplets evaporated at high relative humidity exhibit a freezing of the ring structure at late times. This is evidenced by the plateaus in both the width and mass

evolution of the ring for $H_r \approx 70\%$, (see figures 4 d and e). We also find that, at high humidity, some droplets remain in a liquid state for an extended period, until we abruptly decrease the humidity to that of the ambient at the end of the experiment. A similar behavior at high humidity has been previously observed in droplets of the same composition evaporating on superhydrophobic substrates [40].

This behavior can be explained by the presence of salt. As evaporation proceeds, the salt concentration within the droplet increases until a critical concentration is reached such that $\chi_w(w_s) = H_r$, effectively halting evaporation [40]. Unlike protein-driven evaporation arrest, which is governed by a local condition $\chi_w(w_p) \rightarrow H_r$ near the contact line, salt-induced evaporation arrest is a global phenomenon. This is because the high diffusivity of salt ensures it remains well mixed throughout the droplet, thereby reducing the water activity uniformly and halting evaporation across the entire interface.

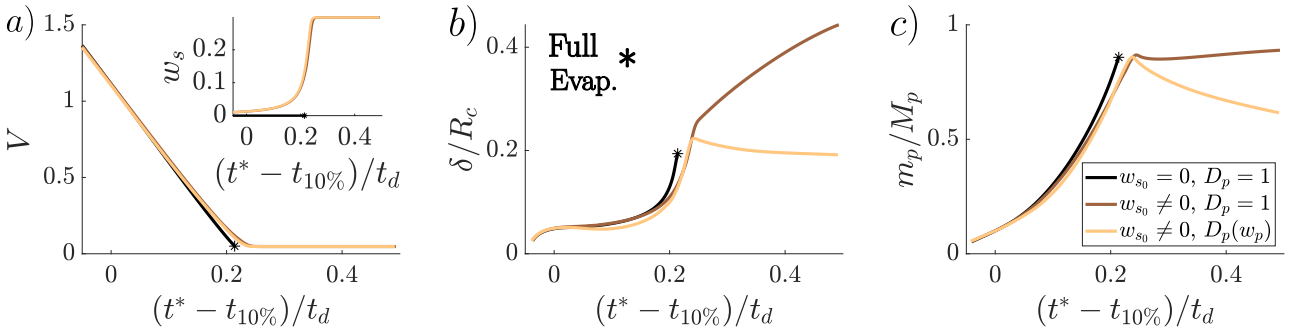


Figure 8: Impact of salt presence and non-constant diffusivity on the morphology of the protein ring at high relative humidity. (a) Temporal evolution of the droplet volume, with the inset showing the corresponding salt mass fraction. (b) Evolution of the protein ring width. (c) Protein mass in the ring normalized by the total protein mass in the droplet. Simulations use parameters $Ca = 10^{-4}$, $Pe = 13.2$, initial protein mass fraction $w_{p0} = 3 \times 10^{-3}$, relative humidity $H_r = 0.7$. Results compare different initial salt mass fractions $w_{s0} = 0, 9 \cdot 10^{-3}$ and constant protein diffusivity $D_p = 1$ and concentration-dependent diffusivity $D(w_p)$.

However, we did not observe the same behavior for all experiments performed at the same conditions of high humidity. Some droplets evaporated completely within the experimental time, while others remained in a liquid state as long as the experiment lasted. This variability arises because the condition $H_r = \chi_w(w_{sc})$ corresponds to a salt concentration w_{sc} above the saturation concentration. Although crystallization is known to occur in evaporating salt-containing droplets at supersaturation [10, 41], the system may remain in a metastable liquid phase once salt concentration is above saturation. In this state, even small fluctuations in ambient relative humidity can trigger efflorescence (i.e., salt crystallization). This delicate balance explains why some droplets at $H_r = 0.7$ crystallize while others remain liquid until the end of the experiment.

To assess the influence of salt, we incorporate into our model an initial salt concentration of $w_{s0} = 9 \cdot 10^{-3}$, as in our experiments. We observe that, under these conditions, droplets evaporating at $H_r = 0.7$ remain stable, but only after the salt mass fraction reaches approximately 0.3 (see figure 8a), a value higher than the saturation mass fraction 0.265. The inclusion of salt in the model also explains the observed plateau in the final stages of the ring mass evolution (see figure 8c). Once evaporation halts due to the condition $\chi_w(w_s) = H_r$, the advective flux that transports solutes toward the contact line disappears. As a result, the solute mass accumulated in the ring remains nearly constant. Interestingly, despite the halt in evaporation, we observe

that the width of the ring continues to increase. This occurs because, in the absence of advective transport, a residual diffusive flux persists, gradually spreading the protein-rich region inward into the droplet. Eventually, this leads to a broadened ring structure that can extend over half of the droplet. However, this behavior is inconsistent with our experimental observations. This discrepancy highlights the limitations of the assumption of constant diffusivity. In reality, protein diffusion is strongly concentration-dependent, especially for concentrated solutions [39, 29], and a more accurate model must account for a non-constant diffusivity to prevent such unrealistic ring broadening.

This result is particularly interesting because, unlike the case of spherical droplets, the formation of a stable polymeric or protein rim in sessile droplets does not necessarily require a concentration-dependent diffusivity for low and medium ambient relative humidity. In spherical droplets, the entire interface becomes uniformly covered by the dense protein shell, effectively halting the apparent advection caused by the receding interface. This shell formation is observed across all values of relative humidity H_r . However, if the diffusivity remains constant, the shell can diffuse inward over a time scale comparable to the evaporation time, given by $t_d = R_c^2/D_p \sim 10^3$ s for a droplet of radius $R_c = 100 \mu\text{m}$ and protein diffusivity $D_p = 10^{-11} \text{ m}^2 \text{ s}^{-1}$.

In contrast, for sessile droplets, the ring formation is not governed by the apparent advection from interface recession but rather by the advective flux required to maintain a pinned contact line and a spherical-cap shape. As a result, the protein ring forms in the vicinity of the contact line, leaving a large portion of the droplet interface free of solute and still contributing to evaporation. Consequently, for low and medium values of H_r , the dependence of the diffusivity on the protein concentration is not critical. As long as the Péclet number satisfies $Pe \gg 1$, the solute accumulates at the rim and salt crystallizes, as evaporation proceeds, before the ring has time to diffuse inward.

However, at high relative humidity, evaporation is globally arrested not due to protein concentration but due to salt concentration, which modifies the water activity such that $\chi_w(w_s) = H_r$ is reached almost uniformly throughout the droplet. Under these conditions, diffusivity plays a crucial role in maintaining a stable ring structure. The diffusive flux must be significantly reduced so that the associated diffusive timescale becomes much longer than the experimental timescale. This is indeed consistent with our experimental findings. When we incorporate a non-constant diffusivity $D_p(w_p)$, which decreases sharply at high protein concentrations (see Section 3.5), we observe that the ring width remains stable over long times (see figure 8 b). This highlights the importance of accounting for concentration-dependent transport properties in modeling the late-stage dynamics of evaporating droplets under high humidity.

4.3 Comparison with experiments

Direct comparisons between experimental measurements and hydrodynamic-solute transport models have not yet been reported for multicomponent droplets. This is mainly due to the experimental difficulty of resolving the spatio-temporal distribution of solvent concentration in evaporating droplets, together with the fact that existing models, developed for particle-laden droplets, fail to capture key features of ring formation in multicomponent solutions. In this section, we compare our model with the experiments presented in Section 2, and discuss its limitations. The model presented in Section 3 contains no free parameters, and whenever possible it relies on material and thermodynamic properties from experimental studies reported in the literature (see Section 3.5).

To enable comparison with experiments, we include salt in our model and account for a non-constant diffusivity. For the dependence of water activity on protein concentration, $\chi_w^p(\bar{w}_p)$, we initially employed the interpolation described in Section 3.5. However, comparison with ex-

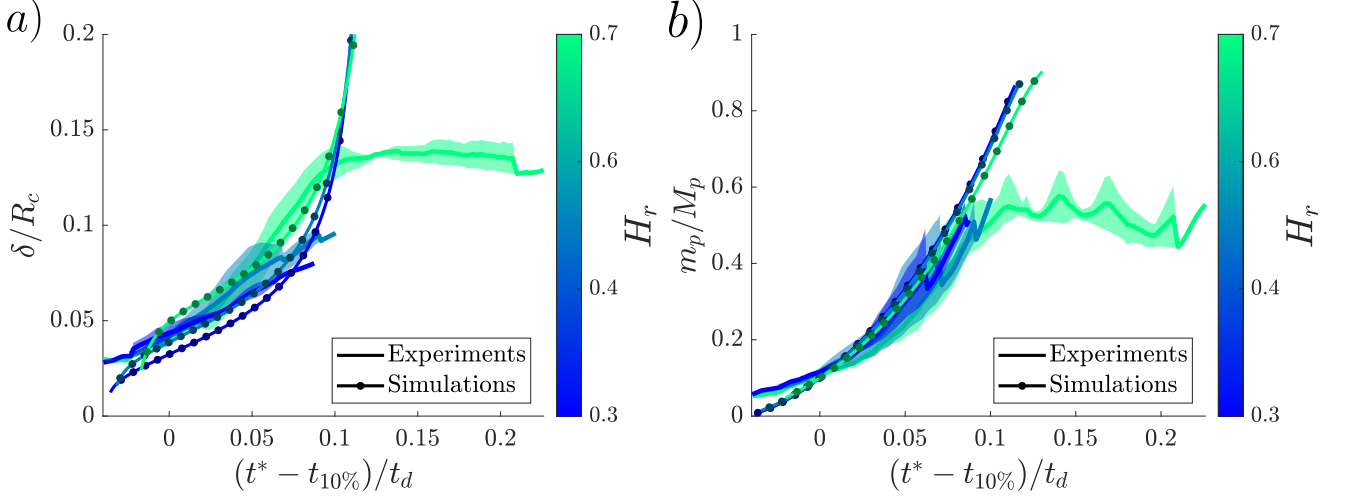


Figure 9: Comparison of experimental results with numerical predictions of our model. The solid line represents the mean of experiments performed at comparable relative humidity, while the shaded region spans the range between the minimum and maximum experimental values. (a) Temporal evolution of the ring width. (b) Temporal evolution of the protein mass in the ring, normalized by the total protein mass in the droplet. The parameters used are $Ca = 10^{-4}$, $Pe = 43.3(1 - H_r)$, relative humidity values $H_r = 0.3, 0.5, 0.7$, concentration-dependent diffusivity $D(w_p)$, initial protein mass fraction $w_{p0} = 3 \cdot 10^{-3}$, and initial salt mass fraction $w_{s0} = 9 \cdot 10^{-3}$.

periments shows that assuming a water activity closer to the ideal case provides much better agreement. Specifically, we borrow the functional form proposed by Salmon *et al.* [39],

$$\chi_w^p = (1 - \bar{w}_p) e^{\bar{w}_p + \xi \bar{w}_p^2}, \quad \text{with} \quad \xi = 0.5 - 3(1 - \bar{w}_p)^{0.09}. \quad (15)$$

The discrepancy may arise because the presence of salt modifies the influence of protein on water activity compared to the salt-free water–mucin measurements of Znamenskaya *et al.* [47]. Additional contributing factors could include differences in the chemical treatment of our mucin or variations in temperature. Therefore, throughout this section we adopt the quasi-ideal water activity model. A discussion of the impact of different water activity formulations on protein ring growth is provided in Appendix 5.

Our model reproduces well the evolution of the protein ring mass (see figure 10b). The evolution of the ring width is also qualitatively reproduced. The model captures the dependence of ring width on relative humidity. Interestingly, at early times it reproduces not only the offset of the curves but also the different slopes observed in the experiments for varying humidity. However, discrepancies arise before crystallization: simulations predict a rapid rim broadening up to the point of salt saturation, whereas experiments show a slower growth. As we discuss in the following section, this mismatch likely results from the simplified rheology assumed in our model, specifically the use of a constant viscosity.

Figure 10a compares the evolution of the height-integrated protein fraction ϕ_p in a representative medium-humidity experiment with the corresponding simulation. The agreement is good until late times, where the *squeezing effect* starts to be present. Both experiments and simulations also show that the maximum in ϕ_p is shifted inward from the droplet edge. However, this effect is significantly weaker in experiments than in simulations.

Our model also captures the observed decrease in maximum height-integrated protein fraction ϕ_p with increasing relative humidity (figure 10b). This trend cannot be explained by constant-

activity models. Finally, the larger experimental variability at medium and low humidity compared to high humidity arises from the limited temporal resolution of our imaging (one frame every five seconds). This uncertainty in identifying the last frame before crystallization introduces dispersion in cases where crystallization occurs while the ring mass is still increasing.

We conclude that our model qualitatively explains the main features of protein rim formation: (i) rim broadening that depends on relative humidity, (ii) similar ring mass evolution across different humidities, (iii) a decrease in the maximum height-integrated protein fraction with increasing humidity. Among these phenomena, constant-activity models account only for the similar evolution of ring mass across humidities. This highlights the need to consider the detailed geometry of the protein rim in order to rationalize experimental findings. Relying solely on the ring mass evolution can be misleading, as it may suggest that growth is a consequence of a maximum protein concentration, whereas in reality rim formation results from the coupling between hydrodynamics and solute transport through the evaporation.

However, the quantitative comparison between experiments and our model reveals a key discrepancy: the ring width is overestimated at late times. This highlights the limitations of our current model. We expect that incorporating more realistic material properties will improve the quantitative agreement with experiments.

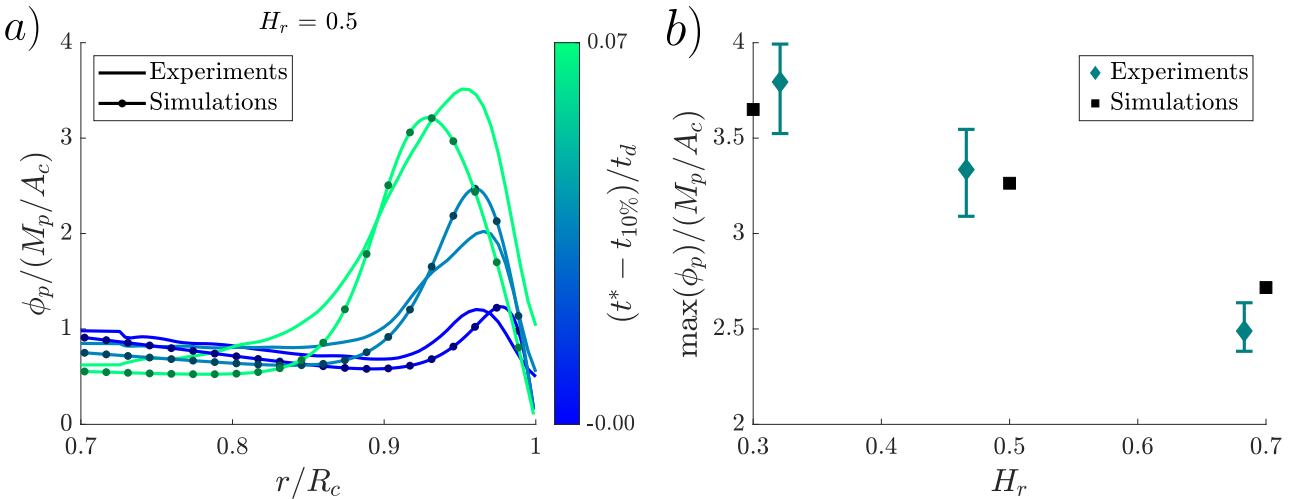


Figure 10: Comparison of experimental results with numerical predictions of our model. (a) Temporal evolution of the height-integrated protein mass fraction, normalized by the total protein mass in the droplet divided by the contact area (b) Maximum height-integrated protein mass fraction, normalized by the total protein mass in the droplet divided by the contact area, as a function of relative humidity. The parameters used are $Ca = 10^{-4}$, $Pe = 43.3(1 - H_r)$, relative humidity values $H_r = 0.3, 0.5, 0.7$, concentration-dependent diffusivity $D(w_p)$, initial protein mass fraction $w_{p0} = 3 \cdot 10^{-3}$, and initial salt mass fraction $w_{s0} = 9 \cdot 10^{-3}$.

4.3.1 Limitations

The rheology of mucin-based solutions is an active area of research [38]. It is well established that the rheological behavior of mucin solutions depends strongly on how they are obtained. Different types of mucin exhibit distinct rheological properties, and chemical treatments can further modify their behavior Georgiades *et al.* [16]. Consequently, the rheological response of our mucin-based solution is not universal and cannot be directly applied to other systems. In some cases, mucin

solutions behave as shear-thinning non-Newtonian fluids, while at higher protein concentrations they may form gels Waigh *et al.* [44], Georgiades *et al.* [16]. In our model, we deliberately avoid this complexity, as our aim is to provide a minimal mechanism to explain the formation of a “coffee-ring” in multicomponent droplets. Nevertheless, one robust feature across rheological studies is that viscosity increases with mucin concentration, and once a critical concentration is reached the solution transitions to a gel-like state with very high viscosity [1, 44, 16]. Incorporating this effect could suppress the *squeezing effect* responsible for the rapid rim broadening observed in our simulations prior to crystallization.

In our current model, viscosity is assumed constant. This implies that throughout evaporation the droplet remains in the low-capillary-number regime, where capillary forces dominate and the droplet shape can be approximated as a spherical cap. Protein accumulation near the contact line eventually suppresses evaporation locally, such that $J \sim 0$. However, the temporal derivative of the height remains nonzero ($\partial h / \partial t \neq 0$) to preserve the spherical-cap geometry. By continuity, this requires a negative flow rate in the region where evaporation is arrested but the interface still recedes, i.e. an inward flow from the contact line towards the center. This produces a reverse advective protein flux that enhances rim thickening (see figure 6b). However, this reverse flow has not been observed in experiments with identical droplet compositions using particle tracking velocimetry [28].

The *squeezing effect* could be suppressed by incorporating a viscosity that increases in a steep way with the protein concentration. Such a dependence is supported by experimental evidence. In fact, viscosity can increase more than four orders of magnitude Bansil *et al.* [1], making the product μCa at least of order unity. Under these conditions, the droplet interface no longer needs to strictly follow a spherical-cap shape, allowing $\partial h / \partial t$ to become negligibly small. As a result, the protein ring can effectively *freeze* with no internal velocities. This would suppress the fast rim broadening driven by the *squeezing effect*. Unfortunately, implementing such a mechanism is not straightforward. A sharp viscosity transition generates steep gradients, which are numerically challenging and can also introduce physical instabilities. In particular, the viscosity jump could induce a local negative curvature, promoting droplet breakup—an effect not observed experimentally. Stabilizing such a system would require including van der Waals forces in the model, adding a level of complexity beyond the scope of this work, which aims to propose a minimal model for the “coffee-ring effect” in multicomponent droplets.

5 Discussion

The coffee-ring effect is one of the most widely studied phenomena in sessile evaporating droplets. The seminal works of Deegan *et al.* [7], Deegan *et al.* [8] brought this effect to the forefront of fluid mechanics research. Since then, more advanced theoretical models have been developed [37, 22, 31, 32, 13, 5], all focused on particle-laden droplets. These models typically assume that the hydrodynamics are decoupled from solute transport. However, as we have demonstrated in this work, such decoupling is not appropriate for multicomponent droplets, where water activity depends on solute concentration, which significantly influences evaporation dynamics.

The widespread recognition of the coffee-ring effect has led to its application in interpreting experimental observations in complex fluids. For instance, Kong *et al.* [23] investigated droplets containing proteins and salts, analyzing their results within the classical particle-based framework. Yet, they reported a linear dependence of ring width on relative humidity—a finding inconsistent with theoretical predictions which suggest that the ring width is independent of hu-

midity. Similarly, Pan *et al.* [36] studied model respiratory droplets with compositions similar to those considered in our work. They also observed a strong relative humidity dependence in both the width and intensity of the protein ring but still interpreted their findings through the lens of particle-laden droplet theory.

Our results provide a natural explanation for these discrepancies. By incorporating a realistic coupling between hydrodynamics and solute transport through an evaporation rate that depends on the local water activity, our minimal model captures key experimental features of complex droplet evaporation. In particular, the dependence of χ_w on solute concentration alone is sufficient to qualitatively reproduce the observed humidity dependence of ring width and intensity. This underscores the importance of including water activity effects in models of complex fluids to accurately predict deposition patterns. Notably, while the classical theory of Popov [37] reproduces the temporal evolution of the ring mass reasonably well, it fails to capture the internal ring structure, including both its thickness and intensity.

Accounting for variations in the protein ring structure is also highly relevant in the context of viral infectivity. Relative humidity is known to influence virus viability in aerosol and droplet residues [33, 25]. In evaporating sessile droplets, this effect must be understood in terms of both the drying dynamics and the composition of the final deposit. Experiments have shown that lower relative humidity leads to thinner protein rings, while higher humidity results in lower peak protein concentrations [23, 36]; see also Section 2. Given that virions have been observed to colocalize with protein-rich regions in dried droplets [36, 28], it is plausible that variations in the protein ring—driven by relative humidity—play a role in modulating viral decay.

In conclusion, although our model is intentionally minimal, it provides a robust framework for capturing key experimental behaviors in complex evaporating droplets. By incorporating water activity-dependent evaporation, we account for the essential coupling between hydrodynamics and solute transport that is overlooked in classical models. We hope this work stimulates further theoretical developments on the coffee-ring effect in multicomponent and biologically relevant systems. A more comprehensive two-dimensional models incorporating additional effects such as Marangoni flows and natural convection have been developed elsewhere [28], but there remains significant potential to extend these approaches across a wider range of compositions and conditions.

Acknowledgements

We are grateful to David Díaz González and Israel Pina García for building the humidity-controlled chamber used in the experiments. We also thank Aránzazu de la Encina, Teresa Bartolomé, Marta Sanz and Fernando Usera for their careful preparation of the protein and salt solutions used in the experiments.

Funding

The authors acknowledge financial support from Grant No. PID2023-146809OB-I00 funded by MICIU/AEI/10.13039/501100011033 and by ERDF/UE and Grant No. PID2020-114945RB-C21 funded by MCIN/AEI/10.13039/501100011033.

Declaration of Interests

The authors report no conflict of interest.

Relevance of Ideal vs. Non-Ideal Water Activity

Merhi *et al.* [29] demonstrated the importance of considering non-ideal water activity in analyzing the equilibrium shape of a spherical respiratory droplet. In an analogous manner, we investigate how the coffee-ring effect is influenced by the functional form of water activity as a function of protein concentration, adopting the empirical relation proposed by Salmon *et al.* [39]:

$$\chi_w = (1 - \bar{w}_p)e^{\bar{w}_p + \xi \bar{w}_p^2},$$

where $\xi = A_{wB} - 3(1 - \bar{w}_p)^{0.09}$. This formulation allows us to tune the non-ideality of the solution through the parameter A_{wB} . When $A_{wB} = 1.5$, the water activity closely approximates that of an ideal mixture, i.e., $\chi_w \approx 1 - \bar{w}_p$. For $A_{wB} = 3.5$, the system becomes strongly non-ideal, with water activity remaining nearly constant at low protein concentrations and dropping sharply only at high concentrations (see figure 11a).

In ideal mixtures, strong differences in ring formation are expected for varying relative humidity (H_r), since the condition $\chi_w(\bar{w}_{p,c}) \approx H_r$ is satisfied at significantly different protein concentrations. This is confirmed by our simulations: for an ideal case ($A_{wB} = 1.5$, dark blue lines in figures 11b and c), the final ring width is about 20% of the droplet radius at $H_r = 0.3$, and nearly 40% at $H_r = 0.7$. In contrast, in the non-ideal case ($A_{wB} = 3.5$), the final ring width is nearly independent of H_r .

The impact of water activity shape is particularly pronounced at high humidity. In an ideal mixture, $\chi_w(\bar{w}_{p,c}) \approx 0.7$ occurs at $\bar{w}_{p,c} \approx 0.3$, whereas for a strongly non-ideal mixture, this condition is only satisfied when $\bar{w}_{p,c}$ is close to 1. At low humidity, this difference is less significant, since even ideal mixtures reach $\bar{w}_{p,c} \approx 1$.

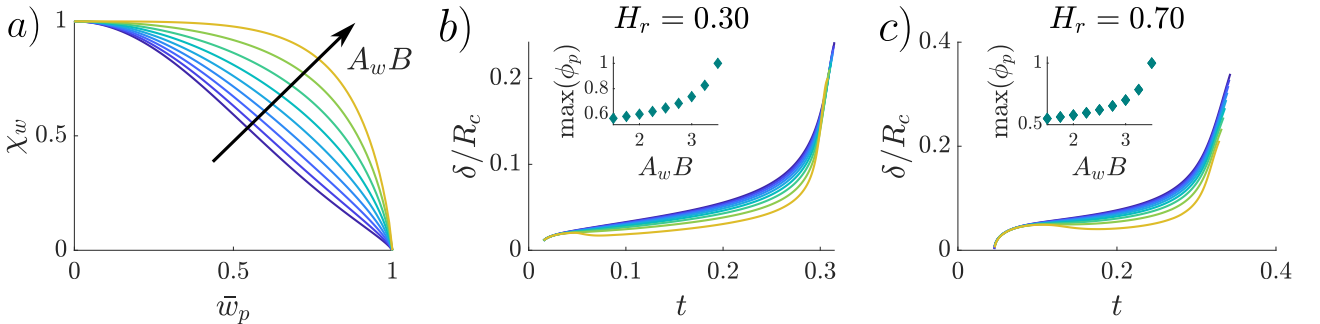


Figure 11: Effect of mixture non-ideality on protein ring morphology. (a) Water activity as a function of protein mass fraction for different values of the non-ideality parameter A_{wB} ranging from 1.5 to 3.5 in steps of 0.25. (b) Temporal evolution of the protein ring width at relative humidity $H_r = 0.3$ for the same A_{wB} values shown in (a). The inset displays the maximum height-integrated protein fraction as a function of A_{wB} . (c) Protein ring width evolution at higher humidity, $H_r = 0.7$, illustrating the impact of humidity on ring morphology under similar non-ideality conditions.

Evaporation Rate

To compute the evaporation rate, we first represent the water activity $\chi_w(r)$ using a cubic spline interpolation. This representation introduces two degrees of freedom at the boundaries of the domain, which must be constrained by appropriate boundary conditions. To ensure physical consistency, we impose symmetry conditions at the droplet center

$$\frac{\partial \chi_w}{\partial r} = 0, \text{ at } r = 0.$$

At the contact line, the derivative is determined by applying the chain rule

$$\frac{\partial \chi_w}{\partial r} = \frac{\partial \chi_w}{\partial w_p} \frac{\partial w_p}{\partial r}, \text{ at } r = 1.$$

Given that the cubic splines are formed by cubic polynomials defined between grid points where the value of χ_w is known, the spline S_{χ_w} can be written as

$$S_{\chi_w}(r) = \sum_{j=0}^3 a_j^i r^j, \text{ for } r \in (r_i, r_{i+1}),$$

where a_j^i is the spline coefficient of the polynomial of order j between grid points i and $i+1$. We can then express $g(r')$ as

$$g(r') = \frac{2}{\pi} \frac{d}{dr'} \left(\sum_{i=0}^L \sum_{j=0}^3 \int_{r_i}^{r_{i+1}} \frac{a_j^i r^{j+1}}{\sqrt{r'^2 - r^2}} dr + \sum_{j=0}^3 \int_{r_{L+1}}^{r'} \frac{a_{L+1}^j r^{j+1}}{\sqrt{r'^2 - r^2}} dr \right),$$

where L is the maximum grid-point such that $r_{L+1} < r'$. This formulation is particularly convenient, as the integrals involved in computing g can be evaluated analytically. Once g is obtained, the evaporation rate J can be computed through numerical integration. For this purpose, we employ Gauss-Kronrod quadrature, as implemented in the `quadgk` function in MATLAB[®]. We verify our implementation by comparing the semi-analytical results with the analytical solution provided by Fu *et al.* [14] for the case in which the water activity χ_w is given by a polynomial function. In figure 12a, we compare the analytical and numerical solutions for $\chi_w = 1 - 0.15 \cdot r^j$, with $j = \{0, 2, 4, 6\}$. It is important to note that, to ensure axisymmetry of the solution, the polynomial order must be even.

Numerical Scheme

Due to the high non-linearity of the thin film equation 10 the spatial discretization must be done carefully. Equations 10 can be written as

$$\frac{\partial(rh)}{\partial t} + \bar{u}_r \frac{\partial(rh)}{\partial r} + rh \frac{\partial \bar{u}_r}{\partial r} = J,$$

We employ a numerical scheme similar to that used by Zheng *et al.* [46], based on two uniform staggered grids: one defined at the primary nodes r_i , and the other at the midpoints $r_{i+1/2}$. A second-order finite difference scheme is applied to approximate spatial derivatives,

$$\frac{\partial h_i}{\partial t} = -\frac{\bar{u}_i}{r_i} \frac{r_{i+1} h_{i+1} - r_i h_i}{r_{i+1} - r_i} - h_i \frac{\bar{u}_{i+1/2} - \bar{u}_{i-1/2}}{(r_{i+1} - r_{i-1})/2},$$

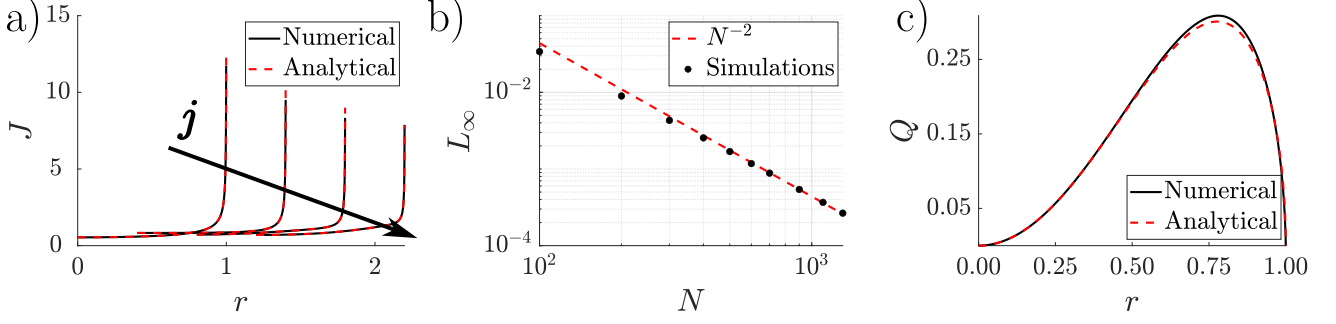


Figure 12: Validation of the numerical framework. (a) Comparison of the semi-analytical evaporation rate with the analytical solution from Fu *et al.* [14] for different polynomial orders $j = 0, 2, 4, 6$. Each curve is shifted by 0.5 along the horizontal axis for clarity. (b) Evolution of the error L_∞ , defined as the maximum deviation from mass conservation during the simulation, plotted against the number of grid points. (c) Comparison of the flow rate predicted by our model with the analytical solution from Gelderblom *et al.* [15], using parameters $Ca = 10^{-4}$, $Pe = 10$, $H_r = 0.5$, and at time $t = 0.1$, early enough to assume $\chi_w \approx 1$.

where

$$\begin{aligned}\bar{u}_i &= \frac{(h_i)^2}{3\mu_i Ca} \frac{p_{i+1} - p_{i-1}}{r_{i+1} - r_{i-1}} \\ \bar{u}_{i+\frac{1}{2}} &= \frac{1}{3Ca(\mu_{i+1} + \mu_i)/2} \left(\frac{h_{i+1} + h_i}{2} \right)^2 \frac{p_{i+1} - p_i}{r_{i+1} - r_i} \\ p_i &= \frac{2}{r_{i+1} - r_{i-1}} \left(\frac{h_{i+1} - h_i}{r_{i+1} - r_i} - \frac{h_i - h_{i-1}}{r_i - r_{i-1}} \right) + \frac{1}{r_i} \frac{h_{i+1} - h_{i-1}}{r_{i+1} - r_{i-1}}.\end{aligned}$$

To discretize spatially the advection-diffusion equation we first defined, following Moore *et al.* [31], the integrated mass variable

$$\Phi_p(r, t) = \int_0^r r' \phi_p(r', t) dr'.$$

In terms of this integrated variable the advection-diffusion equation 11 becomes

$$\frac{\partial \Phi_p}{\partial t} + \left(\bar{u}_r + \frac{1}{Pe} \left(\frac{D_p}{r} + \frac{D_p}{h} \frac{\partial h}{\partial r} \right) \right) \frac{\partial \Phi_p}{\partial r} = \frac{1}{Pe} D_p \frac{\partial^2 \Phi_p}{\partial r^2}.$$

with boundary conditions

$$\Phi_p(0, t) = 0, \quad \Phi_p(1, t) = \frac{1}{4},$$

and initial condition

$$\Phi_p(r, 0) = \frac{r^2}{2} - \frac{r^4}{4}.$$

This equation is discretized using a second-order finite difference scheme at the primary grid nodes r_i . The resulting spatially discretized system of coupled hydrodynamic and transport equations is integrated in time using `ode15s` in MATLAB[®], with a relative tolerance of 10^{-4} and an absolute tolerance of 10^{-7} . We verify the expected second-order spatial convergence of the method through a representative example shown in figure 12b, for a Péclet number $Pe = 30$ and a capillary

number $Ca = 10^{-4}$. In addition, we validate the hydrodynamic implementation by comparing the computed flow rate with the analytical solution reported by Gelderblom *et al.* [15]. This comparison is performed at early times on the evaporation, when the water activity satisfies $\chi_w \approx 1$ (see figure 12c).

References

- [1] BANSIL, RAMA, CAO, XINGXIANG, BHASKAR, K. RAMAKRISHNAN & LAMONT, J. THOMAS 1996 Gelation and aggregation of mucin in relation to the stomach’s protective barrier. *Macromolecular Symposia* **109** (1), 105–113.
- [2] BASU, NANDITA & MUKHERJEE, RABIBRATA 2020 Evaporative drying of sodium chloride solution droplet on a thermally controlled substrate. *The Journal of Physical Chemistry B* **124**, 1266–1274.
- [3] BOULOGNE, FRANÇOIS 2019 Cheap and versatile humidity regulator for environmentally controlled experiments. *The European Physical Journal E* .
- [4] BOULOGNE, FRANÇOIS, INGREMEAU, FRANÇOIS & STONE, HOWARD A 2016 Coffee-stain growth dynamics on dry and wet surfaces. *Journal of Physics: Condensed Matter* **29** (7), 074001.
- [5] COOMBS, NATHAN C. J., SPRITTLES, JAMES E. & CHUBYNSKY, MYKYTA V. 2024 Colloidal deposits from evaporating sessile droplets: Coffee ring versus surface capture. *Phys. Rev. Fluids* **9**, 064304.
- [6] COPSON, E. T. 1947 On the problem of the electrified disc. *Proceedings of the Edinburgh Mathematical Society* **8** (1), 14–19.
- [7] DEEGAN, ROBERT D., BAKAJIN, OLGICA, DUPONT, TODD F., HUBER, GREB, NAGEL, SIDNEY R. & WITTEN, THOMAS A. 1997 Capillary flow as the cause of ring stains from dried liquid drops. *Nature* **389**, 827–829.
- [8] DEEGAN, ROBERT D, BAKAJIN, OLGICA, DUPONT, TODD F, HUBER, GREG, NAGEL, SIDNEY R & WITTEN, THOMAS A 2000 Contact line deposits in an evaporating drop. *Physical review E* **62** (1), 756.
- [9] DEKKER, PIM J., ROCHA, DUARTE, DIDDENS, CHRISTIAN & LOHSE, DETLEF 2025 Internal flow and concentration in neighbouring evaporating binary droplets and rivulets , arXiv: 2508.08820.
- [10] DESARNAUD, JULIE, DERLUYN, HANNELORE, CARMELIET, JAN, BONN, DANIEL & SHAHIDZADEH, NOUSHINE 2014 Metastability limit for the nucleation of nacl crystals in confinement. *The Journal of Physical Chemistry Letters* **5**, 890–895.
- [11] DIDDENS, CHRISTIAN, LI, YAXING & LOHSE, DETLEF 2021 Competing marangoni and rayleigh convection in evaporating binary droplets. *Journal of Fluid Mechanics* **914**.
- [12] DU, FAN, ZHANG, LIYUAN & SHEN, WEI 2022 The internal flow in an evaporating human blood plasma drop. *Journal of Colloid and Interface Science* **609**, 170–178.
- [13] D’AMBROSIO, HANNAH-MAY, WILSON, STEPHEN K., WRAY, ALEXANDER W. & DUFFY, BRIAN R. 2023 The effect of the spatial variation of the evaporative flux on the deposition from a thin sessile droplet. *Journal of Fluid Mechanics* **970**, A1.

- [14] FU, GUANGHUI, CAO, TIESHENG & CAO, LING 2005 On the evaluation of the dopant concentration of a three-dimensional steady-state constant-source diffusion problem. *Materials Letters* **59** (24), 3018–3020.
- [15] GELDERBLOM, HANNEKE, DIDDENS, CHRISTIAN & MARIN, ALVARO 2022 Evaporation-driven liquid flow in sessile droplets. *Soft matter* **18** (45), 8535–8553.
- [16] GEORGIADES, PANTELIS, PUDNEY, PAUL D. A., THORNTON, DAVID J. & WAIGH, THOMAS A. 2014 Particle tracking microrheology of purified gastrointestinal mucins. *Biopolymers* **101** (4), 366–377.
- [17] GREEN, A. E. & ZERNA, W. 1992 *Theoretical Elasticity*, 2nd edn. Dover Publications.
- [18] GUO, WEI, KINGHORN, ANDREW, ZHANG, YAGE, LI, QINGCHUAN, DEY POONAM, ADITI, TANNER, JULIAN & SHUM, HO CHEUNG 2021 Non-associative phase separation in an evaporating droplet as a model for prebiotic compartmentalization. *Nature Communications* **12**.
- [19] HUANG, QISHEN, WANG, WEI & VIKESLAND, PETER J. 2021 Implications of the coffee-ring effect on virus infectivity. *Langmuir* **37** (38), 11260–11268.
- [20] HUISMAN, MAX, DIGARD, PAUL, POON, WILSON C. K. & TITMUSS, SIMON 2023 Evaporation of concentrated polymer solutions is insensitive to relative humidity. *Phys. Rev. Lett.* **131**, 248102.
- [21] KAJIYA, TADASHI, KANEKO, DAISAKU & DOI, MASAO 2008 Dynamical visualization of “coffee stain phenomenon” in droplets of polymer solution via fluorescent microscopy. *Langmuir* **24** (21), 12369–12374.
- [22] KAPLAN, C. NADIR & MAHADEVAN, L. 2015 Evaporation-driven ring and film deposition from colloidal droplets. *Journal of Fluid Mechanics* **781**, R2.
- [23] KONG, ZI-MENG, SANDHU, HARPAL SINGH, QIU, LU, WU, JICHENG, TIAN, WEN-JUN, CHI, XIAO-JING, TAO, ZHI, YANG, CHI-FU JEFFREY & WANG, XIAO-JIA 2022 Virus dynamics and decay in evaporating human saliva droplets on fomites. *Environmental science & technology* .
- [24] LI, Y., YANG, Q., LI, M. & SONG, Y. 2016 Rate-dependent interface capture beyond the coffee-ring effect. *Scientific Reports* **6** (24628).
- [25] LONGEST, ALEXANDRA K, ROCKEY, NICOLE C, LAKDAWALA, SEEMA S & MARR, LINSEY C 2024 Review of factors affecting virus inactivation in aerosols and droplets. *Journal of the Royal Society Interface* **21** (215), 20240018.
- [26] MAILLEUR, ALEXANDRA, PIRAT, CHRISTOPHE, PIERRE-LOUIS, OLIVIER & COLOMBANI, JEAN 2018 Hollow rims from water drop evaporation on salt substrates. *Phys. Rev. Lett.* **121**, 214501.
- [27] MARÍN, ÁLVARO, KARPITSCHKA, STEFAN, NOGUERA-MARÍN, DIEGO, CABRERIZO-VÍLCHEZ, MIGUEL A., ROSSI, MASSIMILIANO, KÄHLER, CHRISTIAN J. & RODRÍGUEZ VALVERDE, MIGUEL A. 2019 Solutal marangoni flow as the cause of ring stains from drying salty colloidal drops. *Physical Review Fluids* **4**, 041601.

- [28] MARTÍNEZ-PUIG, JAVIER, DE LA TORRE LUQUE, CARLOS, ARBESU NIETO, CAROLINA, MARTÍN JOUVE, BEATRIZ, DE LA ENCINA, ARÁNZAZU, BARTOLOMÉ, TERESA, SANZ, MARTA, ALMAZÁN, FERNANDO, OÑA, ANA, USERA, FERNANDO, MARIN, ALVARO & RODRÍGUEZ-RODRÍGUEZ, JAVIER 2025 Viral transport in evaporating sessile model respiratory droplets. *In preparation* .
- [29] MERHI, TANIA, ATASI, OMER, COETSIER, CLÉMENCE, LALANNE, BENJAMIN & ROGER, KEVIN 2022 Assessing suspension and infectivity times of virus-loaded aerosols involved in airborne transmission. *Proceedings of the National Academy of Sciences* **119** (32), e2204593119.
- [30] MIKHAILOV, E., VLASENKO, S., NIESSNER, R. & PÖSCHL, U. 2004 Interaction of aerosol particles composed of protein and salt with water vapor: hygroscopic growth and microstructural rearrangement. *Atmospheric Chemistry and Physics* **4** (2).
- [31] MOORE, MR., VELLA, D. & OLIVER, JM. 2021 The nascent coffee ring: how solute diffusion counters advection. *Journal of Fluid Mechanics* **920**, A54.
- [32] MOORE, MADELEINE ROSE, VELLA, D. & OLIVER, J.M. 2022 The nascent coffee ring with arbitrary droplet contact set: an asymptotic analysis. *Journal of Fluid Mechanics* **940**, A38.
- [33] MORRIS, DYLAN H, YINDA, KWE CLAUDE, GAMBLE, AMANDINE, ROSSINE, FERNANDO W, HUANG, QISHEN, BUSHMAKER, TRENTON, FISCHER, ROBERT J, MATSON, M JEREMIAH, VAN DOREMALEN, NEELTJE, VIKESLAND, PETER J & OTHERS 2021 Mechanistic theory predicts the effects of temperature and humidity on inactivation of sars-cov-2 and other enveloped viruses. *Elife* **10**, e65902.
- [34] NOBLE, B. 1958 Certain dual integral equations. *Journal of Mathematics and Physics* **37** (1-4), 128–136.
- [35] OSWIN, HENRY P, HADDRELL, ALLEN E, OTERO-FERNANDEZ, MARA, MANN, JAMIE FS, COGAN, TRISTAN A, HILDITCH, THOMAS G, TIAN, JIANGHAN, HARDY, DANIEL A, HILL, DARRYL J, FINN, ADAM & OTHERS 2022 The dynamics of sars-cov-2 infectivity with changes in aerosol microenvironment. *Proceedings of the National Academy of Sciences* **119** (27), e2200109119.
- [36] PAN, JIN, DUGGAL, NISHA K, LAKDAWALA, SEEMA S, ROCKEY, NICOLE C & MARR, LINSEY C 2025 Mucin colocalizes with influenza virus and preserves infectivity in deposited model respiratory droplets. *Environmental Science & Technology* .
- [37] POPOV, YURI O. 2005 Evaporative deposition patterns: Spatial dimensions of the deposit. *Phys. Rev. E* **71**, 036313.
- [38] RULFF, HANNA, SCHMIDT, ROBERT F., WEI, LING-FANG, FENTKER, KERSTIN, KERKHOFF, YANNIC, MERTINS, PHILIPP, MALL, MARCUS A., LAUSTER, DANIEL & GRADZIELSKI, MICHAEL 2024 Comprehensive characterization of the viscoelastic properties of bovine submaxillary mucin (bsm) hydrogels and the effect of additives. *Biomacromolecules* **25** (7), 4014–4029.

- [39] SALMON, JEAN-BAPTISTE, DOUMENC, FRÉDÉRIC & GUERRIER, BÉATRICE 2017 Humidity-insensitive water evaporation from molecular complex fluids. *Phys. Rev. E* **96**, 032612.
- [40] SEYFERT, CAROLA, RODRÍGUEZ-RODRÍGUEZ, JAVIER, LOHSE, DETLEF & MARIN, ALVARO 2022 Stability of respiratory-like droplets under evaporation. *Physical review fluids* **7** (2), 023603.
- [41] SHAO, XIAOXIAO, HOU, YU & ZHONG, XIN 2021 Modulation of evaporation-affected crystal motion in a drying droplet by saline and surfactant concentrations. *Colloids and Surfaces A: Physicochemical and Engineering Aspects* **623**, 126701.
- [42] THAYYIL RAJU, LIJUN, DIDDENS, CHRISTIAN, RODRÍGUEZ-RODRÍGUEZ, JAVIER, VAN DER LINDEN, MARJOLEIN N., ZHANG, XUEHUA, LOHSE, DETLEF & SEN, UDDALOK 2024 Evaporation of binary liquids from a capillary tube. *Journal of Fluid Mechanics* **983**, A21.
- [43] VEJERANO, ERIC P & MARR, LINSEY C 2018 Physico-chemical characteristics of evaporating respiratory fluid droplets. *Journal of The Royal Society Interface* **15** (139), 20170939.
- [44] WAIGH, T. A., PAPAGIANNOPOULOS, A., VOICE, A., BANSIL, R., UNWIN, A. P., DEWHURST, C. D., TURNER, B. & AFDHAL, N. 2002 Entanglement coupling in porcine stomach mucin. *Langmuir* **18** (19), 7188–7195.
- [45] WARDZALA, CASIA L., WOOD, AMANDA M., BELNAP, DAVID M. & KRAMER, JESSICA R. 2022 Mucins inhibit coronavirus infection in a glycan-dependent manner. *ACS Central Science* **8** (3), 351–360.
- [46] ZHENG, ZHONG, FONTELOS, MARCO A., SHIN, SANGWOO, DALLASTON, MICHAEL C., TSELUIKO, DMITRI, KALLIADASIS, SERAFIM & STONE, HOWARD A. 2018 Healing capillary films. *Journal of Fluid Mechanics* **838**, 404–434.
- [47] ZNAMENSKAYA, YANA, SOTRES, JAVIER, ENGBLOM, JOHAN, ARNEBRANT, THOMAS & KOCHERBITOV, VITALY 2012 Effect of hydration on structural and thermodynamic properties of pig gastric and bovine submaxillary gland mucins. *The Journal of Physical Chemistry B* **116**, 5047–5055.